Dynamics of fault-fluid-hydrate system around a shale-cored anticline in deepwater Nigeria

N. Sultan,[1] V. Riboulot,[1] S. Ker,[1] B. Marsset,[1] L. Géli,[1] J. B. Tary,[1] F. Klingelhoefer,[1] M. Voisset,[1] V. Lanfumey,[1] J. L. Colliat,[2] J. Adamy,[3] and S. Grimaud[2]

[1] Gas hydrates were recovered by coring at the eastern border of a shale-cored anticline in the eastern Niger Delta. To characterize the link between faults and fluid release and to identify the role of fluid flow in the gas hydrate dynamics, three piezometers were deployed for periods ranging from 387 to 435 days. Two of them were deployed along a major fault linked to a shallow hydrocarbon reservoir while the third monitored the fluid pressure in a pockmark aligned above the same major fault. In addition, 10 ocean-bottom seismometers (OBS) were deployed for around 60 days. The piezometers simultaneously registered a prolonged fluid flow event lasting 90 days. During this time, OBS measurements record several episodic fluid release events. By combining and analyzing existing and newly acquired data, we show that the fluid-fault system operates according to the following three stages: (1) upward pore fluid migration through existing conduits and free gas circulation within several shallow sandy layers intersecting the major fault, (2) gas accumulation and pore pressure increases within sandy-silty layers, and (3) hydrofracturing and fluid pressure dissipation through sporadic degassing events, causing pore fluid circulation through shallow sandy layers and drawing overlying seawater into the sediment. This paper clearly demonstrates how an integrated approach based on seafloor observations, in situ measurements, and monitoring is essential for understanding fault-fluid-hydrate systems.

Citation: Sultan, N., et al. (2011), Dynamics of fault-fluid-hydrate system around a shale-cored anticline in deepwater Nigeria, *J. Geophys. Res.*, *116*, B12110, doi:10.1029/2011JB008218.

1. Introduction

[2] The Niger Delta is an active area for the oil industry, and many seep-related seabed features have been found recently, particularly during exploration mapping at water depths between 500 and 1500 m [*Hovland et al.*, 1997; *Brooks et al.*, 2000; *Georges and Cauquil*, 2007; *Sultan et al.*, 2010]. Studies from the Nigerian continental slope have shown a broad range of seafloor sedimentary features such as pockmarks, slides, and carbonate buildups associated with fluid flow and gas hydrates [e.g., *Damuth*, 1994; *Cohen and McClay*, 1996; *Brooks et al.*, 2000; *Haskell et al.*, 1999; *Hovland et al.*, 1997; *Deptuck et al.*, 2003; *Bayon et al.*, 2007; *Georges and Cauquil*, 2007; *Sultan et al.*, 2007]. These observations make the Niger Delta an important source of hazards for deepwater infrastructure but also a prime target for studying the active interplay of fluid flow processes, gas hydrate dynamics and seafloor deformation.

[3] The study area discussed here is located in the eastern Niger Delta. Given the temperature and pressure conditions of the study site and the geophysical evidence of free gas infiltration through fault networks to the shallow subsurface, gas hydrates were considered to be a major hazard. Understanding the fault-fluid-hydrate system requires an integrated approach combining detection and quantification of gas hydrate with monitoring of the fluid system controlling gas hydrate stability. Within the context of hazard assessment associated with the occurrence of free gas and gas hydrates in the study area and in order to evaluate the impact of the fault-fluid-hydrate systems on seabed engineering structures, the main objectives of the present work are to (1) evaluate the dynamics (active or not) of the fault-fluid-hydrate system and (2) determine links among fault activities, free gas release, and hydrate accumulation.

2. Tools and Methods

[4] Geotechnical, geophysical, and geological data used in this work were acquired within the framework of a joint research and development project (called ERIG3D) between Ifremer and Total in 2008. Sediment samples were collected in the study area using piston corers. In situ geotechnical measurements were carried out using the Ifremer piezocone (or CPTu for cone penetration test with additional

[1]Département Géosciences Marines, Ifremer, Plouzané, France.
[2]Total, Pau, France.
[3]Total, Paris, France.

measurement of the porewater pressure). The Ifremer pie-zocone is equipped with a rod that penetrates the sediment to a maximum depth of 30 m (for more details see *Sultan et al.* [2010]). The Ifremer piezometer was also used to measure the in situ pore pressure during the ERIG3D cruise. It is a free-fall device with a sediment-piercing lance attached to a recoverable instrument part (for more details see *Sultan et al.* [2010]). Also, 10 ocean-bottom seismometers (OBS) were deployed in the study area for a duration of 2 months. The OBSs were designed to record very small events using externally deployed geophones to ensure good seafloor coupling. Calypso cores, piezocones, piezometers, and OBS characteristics are presented in Tables E1–E4 (Appendix E).

[5] The high-resolution 3-D seismic data used in this study were provided by Total. The in-line spacing of the traces is 6.25 m, and the cross-line spacing is 12.5 m. The dominant frequency is 70 Hz in the upper 100 ms, giving a vertical resolution of ~10.5 m (at a velocity of 1500 m/s). Complementary, high-resolution deep-tow seismic data were acquired during the ERIG3D cruise using the recently developed SYSIF deep-towed acquisition system [*Marsset et al.*, 2010; *Ker et al.*, 2010]. SYSIF is a deep-towed instrument hosting low-frequency acoustic transducers (250–1000 and 650–2000 Hz) and a single channel streamer in order to provide high-resolution (HR) images of the subbottom.

3. Seafloor and Subseafloor Characterization

[6] The Niger Delta margin is undergoing deformation by gravity-driven tectonism that is due to the presence of a mobile substratum at the base of the sediment fill [*Bilotti and Shaw*, 2005; *Corredor et al.*, 2005; *Damuth*, 1994]. The offshore part of the Niger Delta can be divided into several structural zones. The continental shelf is characterized by an extensional zone [*Damuth*, 1994], dominated by listric normal faults (synthetic and antithetic) with extensive growth [*Morley and Guerin*, 1996]. The upper and middle parts of the slope are characterized by a translational zone [*Damuth*, 1994] dominated by folding and faulting in response to rapid sedimentation rates and shale remobilization [*Doust and Omatsola*, 1990; *Morley and Guerin*, 1996]. As the thick stratigraphic column moved downslope [*Morley and Guerin*, 1996], the lower slope is characterized by a compressional zone [*Damuth*, 1994] dominated by a series of linear toe thrusts forming a fold-and-thrust belt. The study site is located in the northeastern Gulf of Guinea on the continental slope of the modern Niger Delta (in the translational zone). The site is about 100 km offshore on the eastern Niger Delta margin coastline at water depths ranging from 700 to 800 m (Figure 1a). The investigated area is located to the northeast of a shale-cored anticline with relief of 48 m (Figure 1b) and is characterized by the presence of several structures and features linked to fluid activities: (1) a series of fault scarps to the north and the south of the anticline, (2) seafloor undulations around the central anticline and numerous pockmarks and irregular depressions on the north and south sides of the anticline (Figures 1c and 2) and (3) a bottom-simulating reflector (BSR) that could be associated with the occurrence of gas hydrates and underlying free gas.

3.1. Faults

[7] The geological interpretation of the study area is based on a set of very high resolution (VHR) bathymetry data and the 3-D exploration seismic data. The study site displays various recent and active processes such as slope failures, deformation, and fluid escape, as demonstrated by a broad variety of pockmarks (Figures 1 and 2). The very detailed bathymetric data presented in Figure 2a reveal the presence of two pockmark fields separated by a major E-W structural fault (in the following called the major eastern fault). The stratigraphic interpretation of the 3-D seismic data has been used to compile a map of buried structural faults (Figure 2b) and a very high resolution geomorphologic map presented in Figure 2c.

[8] The geological structure of the study area reveals a fault system composed of numerous (15) extrados faults related to the uplift of the shale anticline (Figure 2b). From these 15 long-term growth faults, only 1 fault seems active and is marked on the seafloor by a large depression (dark blue in Figure 2c) and at depth by an offset of the most recent sedimentary layers (>20 m for the D20 reflector: from around 25 mbsf to around 45 mbsf, as shown in Figure 3). This major fault intersects a deep hydrocarbon reservoir and is suspected to be the central conduit of the studied fault-fluid-hydrate system. The others faults, which are normal faults, are buried under a minimum of 100 m of undisturbed sediments.

3.2. Pockmarks

[9] The seafloor morphology of the study site is also characterized by several subcircular depression features. These range from a few meters to 250 m in diameter and are probably the result of fluid seepage. Newly acquired and existing seismic data permit different types of pockmarks in the study area to be distinguished [*Riboulot et al.*, 2011]. Various shapes identified from the seafloor bathymetry and deep structures underneath indicate different geological processes at the origin of the observed pockmarks: (1) dewatering, (2) buried mass transport deposits, (3) active faulting, and (4) fluid escape from petroleum reservoirs. A fifth type of pockmark can be directly linked to the presence of gas hydrates and is probably associated with the dynamics of the hydrate system (Figure 2c). These hydrate-associated pockmarks have a distorted shape with boundaries less well defined than pockmarks commonly described in literature examples. Gas hydrates were recovered by coring from some of those pockmarks, while for other pockmarks, gas hydrates were inferred based on the analyses of seismic and bathymetric data.

3.3. Gas Hydrate Occurrence

[10] Figure 3a shows the seismic profile SY08THR-Pr05 that crosses the major eastern fault (labeled "MNF") to the south. One of the main features observed in this seismic profile and indicated in Figure 3a corresponds to the presence of a discontinuous reflector crossing sediment layers between SP 1520 and SP 2000 (see also Figure A1). In order to determine the significance of this reflector, several in situ piezocone measurements (Figures 1b and 3a and Table E2) were carried out along and close to the SY08THR-Pr05 profile.
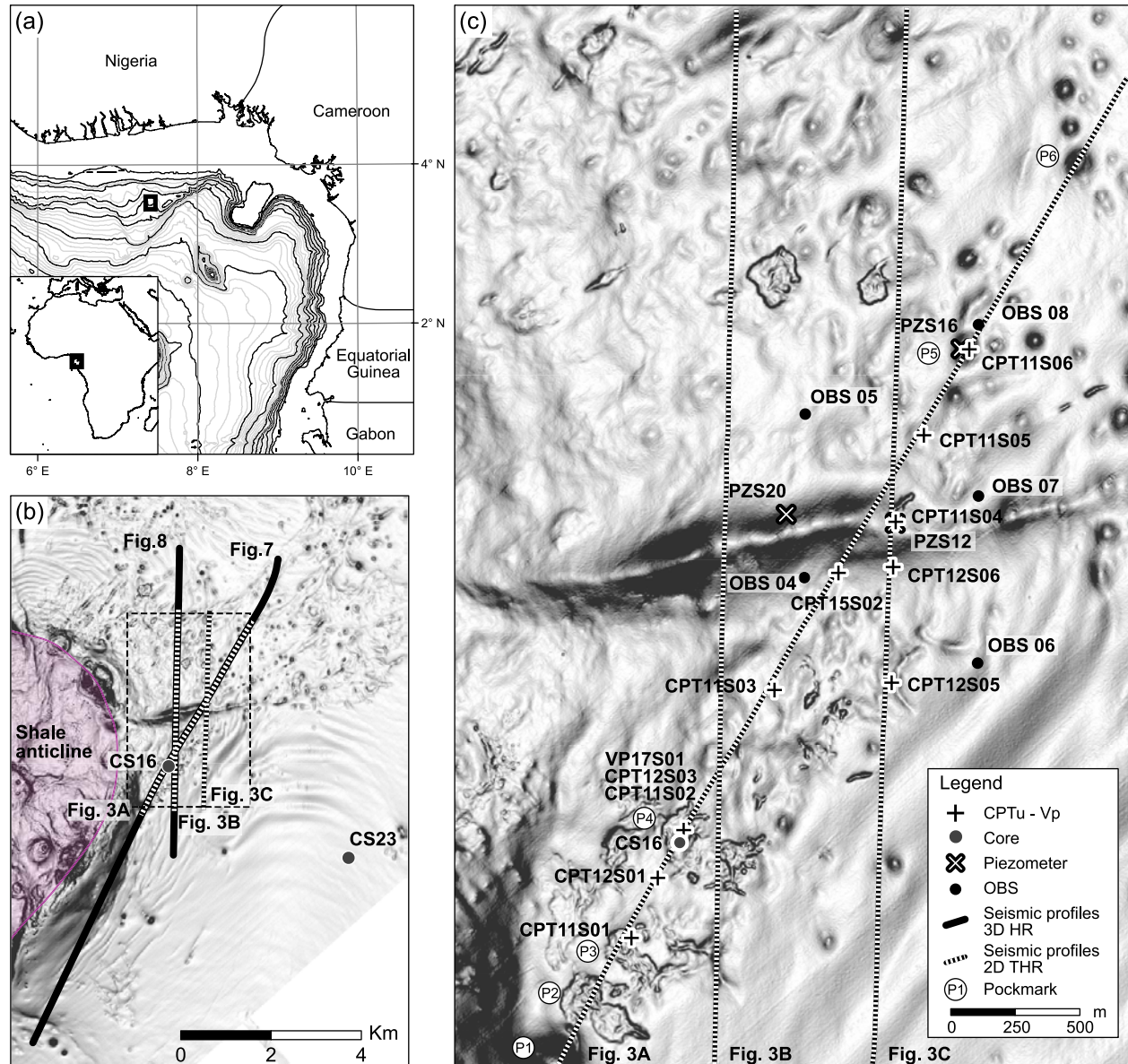
Figure 1. Location maps: (a) Gulf of Guinea general bathymetry map and location of the study area on the Niger Delta deep province (bathymetric contour spacing is 100 m); (b) dip map of the study area (horizontal resolution of the map is 3 m); (c) zoom on the main irregular pockmarks and on the major normal structural fault (see location in Figure 1b).

[11] Piezocone measurements carried out within the NERIS project [*Sultan et al.*, 2007] show that the distinction between gas hydrates and carbonate concretions or sandy-silty layers is possible using the measured excess pore pressure (Δu_2) during piezocone rod penetration. While high excess pore pressure was generated during piezocone testing in gas-hydrate-bearing areas, a low excess pore pressure (in some cases lower than the hydrostatic pressure) was generated by piezocone testing in areas bearing carbonate concretions. Moreover, high Δu_2 with normal corrected cone resistance values can be an indicator of the presence of free gas. Based on these previous observations, piezocone data presented in Figures 4 and 5 were interpreted in terms of sandy-silty layers, gas hydrates, and free gas. Moreover, a

calypso core recovered from above the horizontal reflector indicated in Figure A1 as an indicator of the top of the GHOZ (location in Figure 1b) confirmed the presence of gas hydrates in the area (see Figure A2).

4. Fluid Conduits and Subsurface Fluid Circulation

4.1. Sandy and Fractured Clayey Layers as Fluid Conduits

[12] The VHR seismic profiles (Figure 3) show several continuous reflectors characterized by high amplitude (*Dxx*). 3-D seismic data show the continuity of those reflectors in the complete study area (regional reflectors). In situ
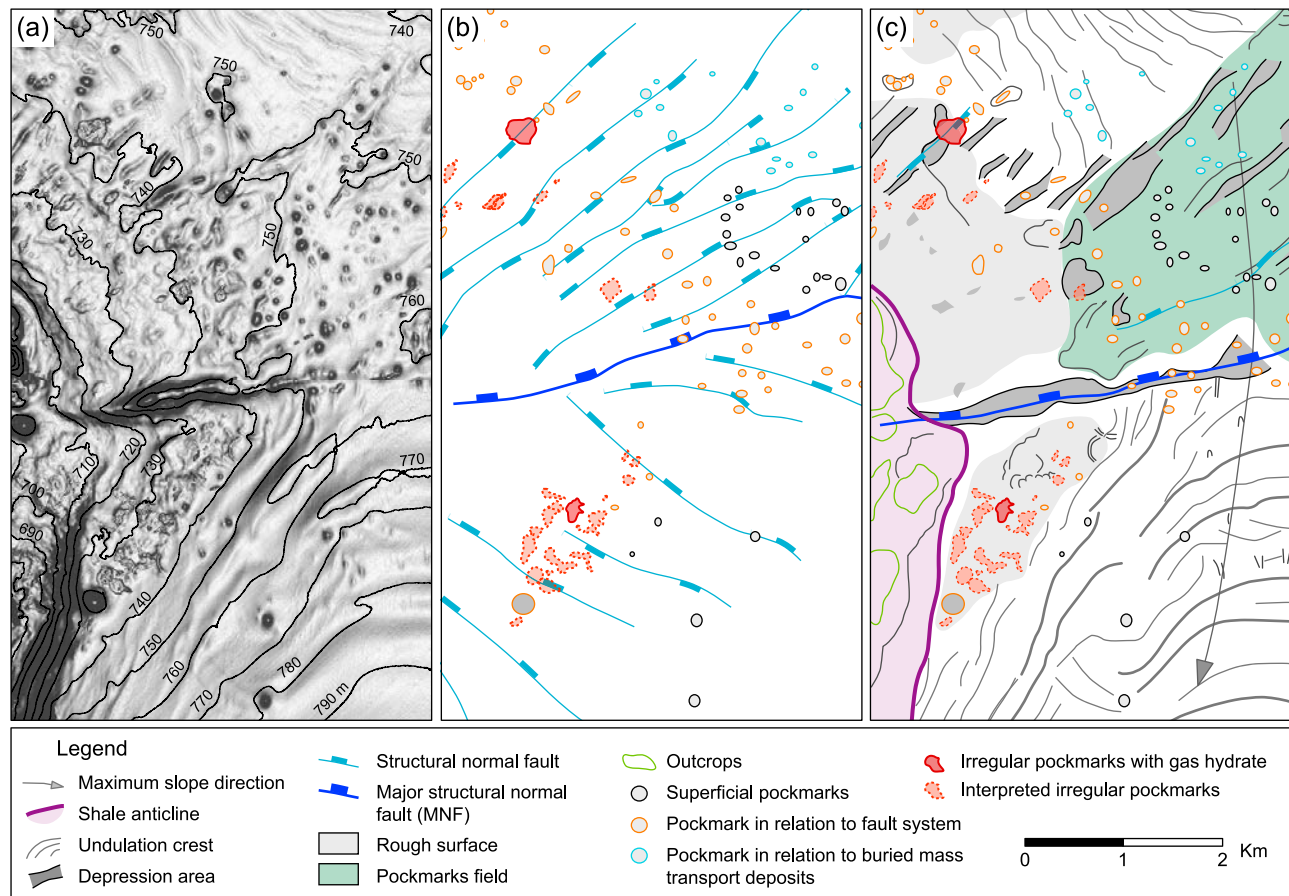
Figure 2. Seafloor and subseafloor characterization: (a) dip map (10 m spaced bathymetric lines), (b) structural map showing normal fault system that is due to growth fold and the actual seafloor fluid seepage, (c) seismic geomorphologic map.

piezocone data have shown that the high-amplitude reflectors named D50 and D30 also correspond to sandy-silty layers, which are characterized by high tip resistance, high friction, and low pore pressure (see CPT11S02, CPT11S05, and CPT11S06 data in Figure 5 and Appendix A). In the following, the Dxx reflectors presented in Figure 3 are interpreted as sandy-silty layers by extension of observations concerning D50 and D30. The distribution of the sandy layers within and surrounding the major eastern fault is important for the understanding of the activity of the whole system going from the reservoir to the subsurface sedimentary layers. Indeed, the high permeability of those sandy layers makes them act as conduits for fluid flow. Almost all the gas hydrates and free gas layers were detected above silty-sandy layers, as can be observed from Figures 4 and 5, further confirming the role of sandy layers serving as conduits for fluid flow.

[13] Figure 6 compares the corrected cone resistance versus depth from two different sites in the south (CPT12S06) and in the central part (CPT11S04) of the major eastern fault. The qt values between the seabed and 9.5 mbsf fit well between the two sites. The sandy-silty layers seem distributed at different depths between CPT12S06 and CPT11S04, probably as a result of the fault movements (Figure 6). Another interesting observation from Figure 6 is the reduced qt values (around 50% with respect to CPT11S04) between

10 and 16 mbsf for CPT12S06. This rapid qt decrease could indicate of the presence of weak or fractured zones at CPT12S06. These weak or fractured zones are also located above sandy-silty layers, suggesting that fluid circulation may occur at the border of the fault by fracturing the superficial clayey layers.

4.2. Fluid Flow

[14] To understand fluid seep processes and associated features observed on the seafloor and in the superficial sediments (Figure 2), it is important to have a good understanding of the system from the deep structure to the upper sedimentary layers. This information can be extracted from 3-D seismic blocks and VHR seismic profiles, which allow the superficial fluid migration just beneath the seafloor in the gas hydrate stability zone (GHSZ) to be inferred. In situ geotechnical properties, pore pressure monitoring, and ocean-bottom seismometer (OBS) recording may complement the seismic interpretation by providing a quantitative approach.

4.2.1. Evidence From 3-D Seismic Data

[15] The shale anticline (purple in Figure 7 and Figure 8) that has been identified beneath the major eastern fault is presented in Figure 2. The shallow undeformed sediments serve to trap fluids in the anticline core. Some sedimentary layers, marked by gray in the two seismic profiles in
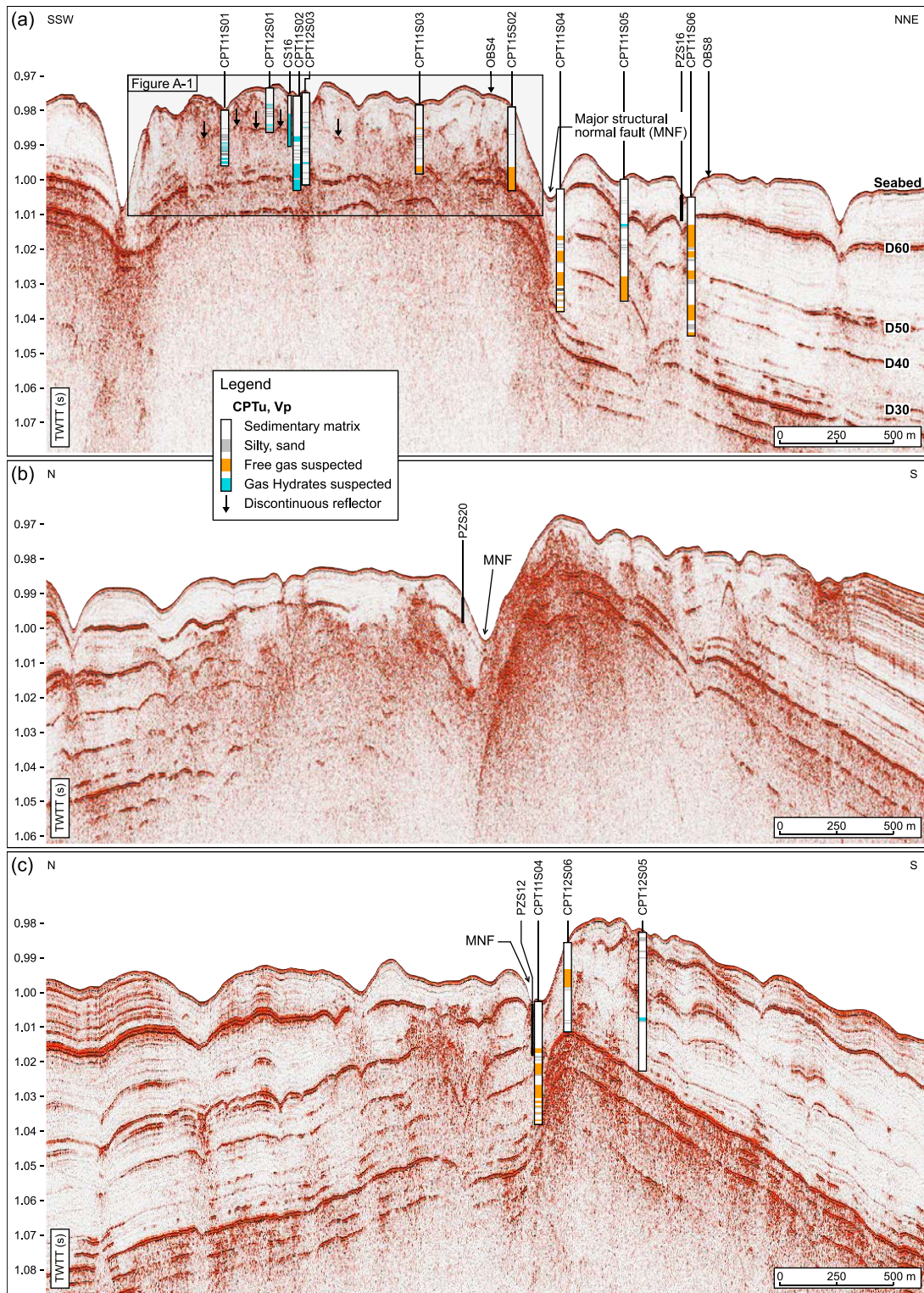
Figure 3. Uninterpreted 2-D very high resolution seismic profiles with interpreted piezocone data: (a) profile SY08THR-Pr05, (b) profile SY08THR-Pr02, (c) profile SY08THR-Pr03. The high-amplitude reflectors named *Dxx* are interpreted from coring and in situ measurements like coarse grain layers (see Appendix A).
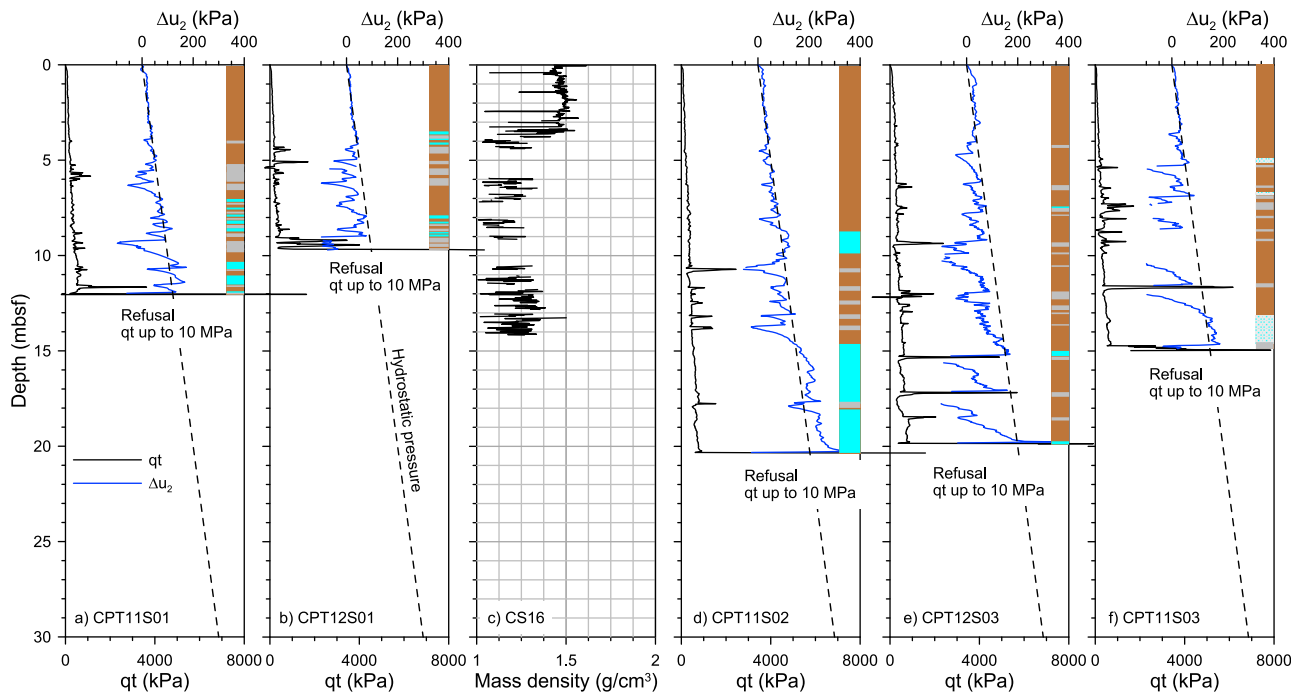
Figure 4. Corrected cone resistance qt and excess pore pressure Δu_2 versus depth from sites (a) CPT11S01, (b) CPT12S01, (d) CPT11S02, (e) CPT12S03, and (f) CPT11S03. (c) Mass density values versus depth from core CS16. Brown areas correspond to soft clay, gray dashed areas correspond to suspected silty-sandy layers, dark blue areas correspond to gas hydrates, and light blue areas correspond to free gas.
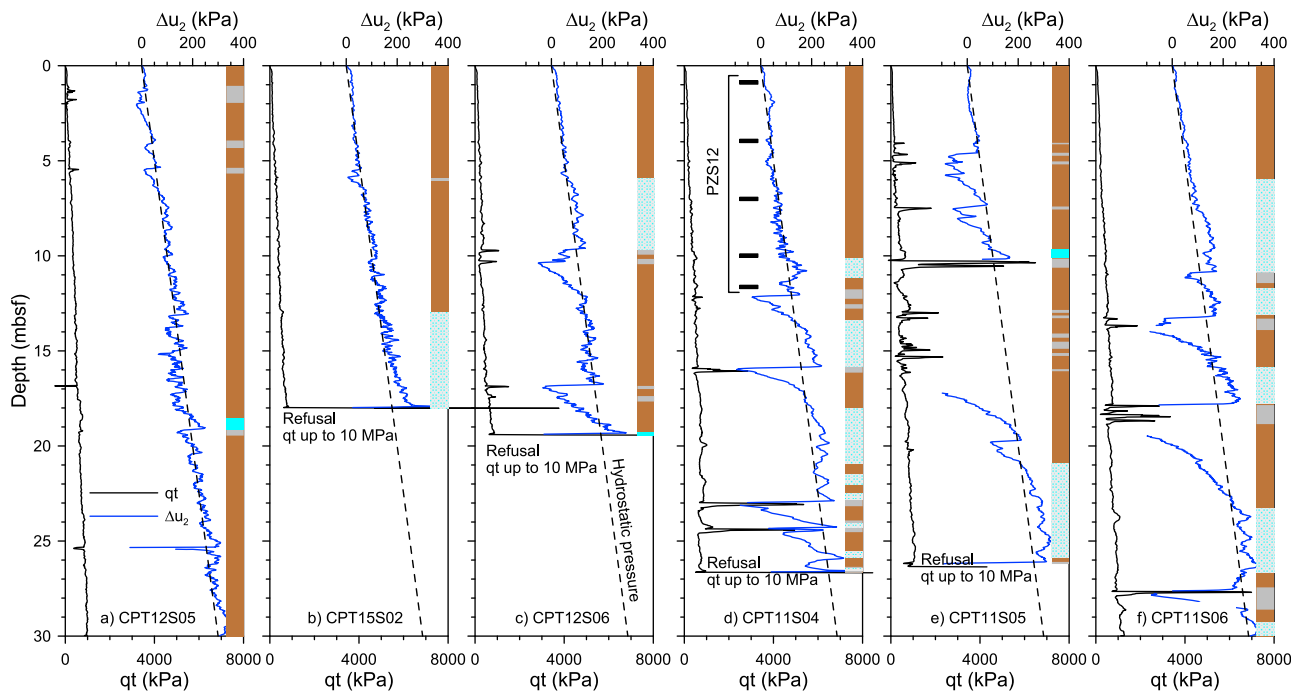

Figure 5. Corrected cone resistance qt and excess pore pressure Δu_2 versus depth from sites (a) CPT12S05, (b) CPT15S02, (c) CPT12S06, (d) CPT11S04, (e) CPT11S05, and (f) CPT11S06. Brown areas correspond to soft clay, gray dashed areas correspond to suspected silty-sandy layers, dark blue areas correspond to gas hydrates, and light blue areas correspond to free gas. Depth position of the PZS12 sensors are shown in Figure 5d.
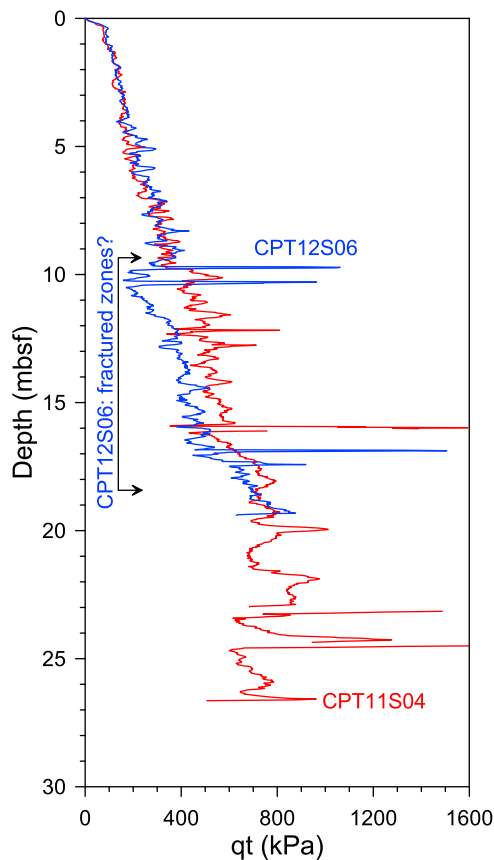
Figure 6. Corrected cone resistance qt versus depth from sites CP12S06 and CPT11S04. These sites are separated by 115 m, yet have identical qt values down to 9.5 mbsf. Reduced qt values at CP12S06 may indicate a zone in which fluid circulation at the fault border is fracturing clayey layers.

Figures 7b and 8b, are characterized by high-amplitude reflectors indicating the possible location of fluid flows. Many of the normal structural faults presented previously on the dip map in Figure 2 are also indicated on the 3-D seismic data in Figures 7b and 8b. The connection between the reservoirs (main deep reservoir and intermediate reservoirs) and these extrados faults shows the path fluids may follow. Indeed, the long-term growth fault acts as the main hydrocarbon migration pathway [*Zhang et al.*, 2006]. The fault system serves as a preferential conduit for fluid flow toward the seafloor, analogous to observations by *Papatheodorou et al.* [1993] and *Bøe et al.* [1998]. In the shallow sediment, the silty-sandy layers and hydrofractured clayey layers also serve as secondary fluid conduits. Intermediate fluid reservoirs in the Plio-Quaternary canyon also can be observed from the 3-D seismic data (Figure 7b). This Plio-Quaternary canyon is filled by reworked heterogeneous sediments with many fissures and cracks (chaotic facies in Figure 7b). These intermediate reservoirs are directly connected to the major eastern fault.

[16] The 3-D seismic profile presented in Figure 8b gives important information regarding the presence of fluid near the seafloor. A high-amplitude reflection parallel to the seafloor with a reverse polarity compared with the seafloor

reflection, located at around 100 ms twtt below the seafloor is interpreted as a BSR. 3-D seismic data presented in Figures 7a and 8a give important information about the intermediate reservoirs and fluid conduits, although these data are not accurate enough to provide a framework for understanding the fluid migration processes and trajectories in the shallower sedimentary layers.

4.2.2. Evidence From VHR Seismic Data

[17] Subsurface amplitude anomalies observed from the VHR seismic profiles presented in Figure 3 suggest the occurrence of high fluid flows. The gas front (chaotic facies) identified from VHR seismic profiles suggests fluid that migrates along the structural faults must diffuse laterally through natural conduits (Figures 7c and 8c). Reflectors *Dxx*, which were identified from VHR profiles (Figure 3a), correspond to highly permeable silty-sandy layers that may serve as lateral fluid conduits. This lateral transmission of fluid seems to control the repartition of fluid flow below the seafloor in the vicinity of faults. Figure 8c shows that fluid flow can also cross the upper clayey layers by hydrofracturing and drain fluid directly at the seabed level. This observation was already drawn from the piezocone data CPT12S06 in which hydrofractured sediments were detected by the important decreases of qt values between 10 and 16 mbsf (Figure 6). Fluid flow may have been important in the generation of the pockmarks denoted *Px* in Figures 7c and 8c and also in the generation of the gas hydrates. A nonconsistent high-amplitude reflector indicated in Figure 7c just underneath P4 could highlight the top of gas hydrates as presented in Appendix A. Indeed, the simultaneous presence of free gas and gas hydrate results in a large velocity contrast marked by the high-amplitude reflector in geophysical data. Furthermore, gas hydrates were recovered in this area (Appendix A) and were suspected using in situ piezocone data. VHR seismic data confirmed the link between fluid migration in the subsurface through faults and sandy-silty layers, gas hydrate accumulations, and several pockmark locations.

4.2.3. Evidence From Piezometer Measurements

[18] A total of three long-term piezometers measurements were carried out at three different locations surrounding the major eastern fault (PZS12, PZS16, and PZS20; Figure 1). In the following, only PZS12 and PZS20 data (Figures 9 and 10) are presented and discussed. Indeed, data from PZS16 did not show any significant changes in terms of pore pressure measurements.

[19] In Figure 5d, the five pressure sensor locations of PZS12 are projected onto the piezocone data from site CPT11S04. The upper four sensors of PZS12 are positioned in clayey sediments while the fifth one is just above a sandy-silty layer that is characterized by high tip resistance and almost zero Δu_2.

[20] Figure 9a presents, for PZS12, the initial impulsion and dissipation of the pore water pressure at the five sensor levels. Between 36 and 48 h were needed to reach the pore pressure equilibrium of all five sensors. For the upper four sensors (P1–P4), pore pressures remained almost constant until the end of the deployment (Figure 9a). The P5 sensor was located at 11.48 mbsf, directly above a coarse sediment layer, as can be observed from the CPT1104 data (which vary significantly with time; see Figure 5). For PZS12/P5, the differential pore pressure increases slightly (by ~1 kPa)
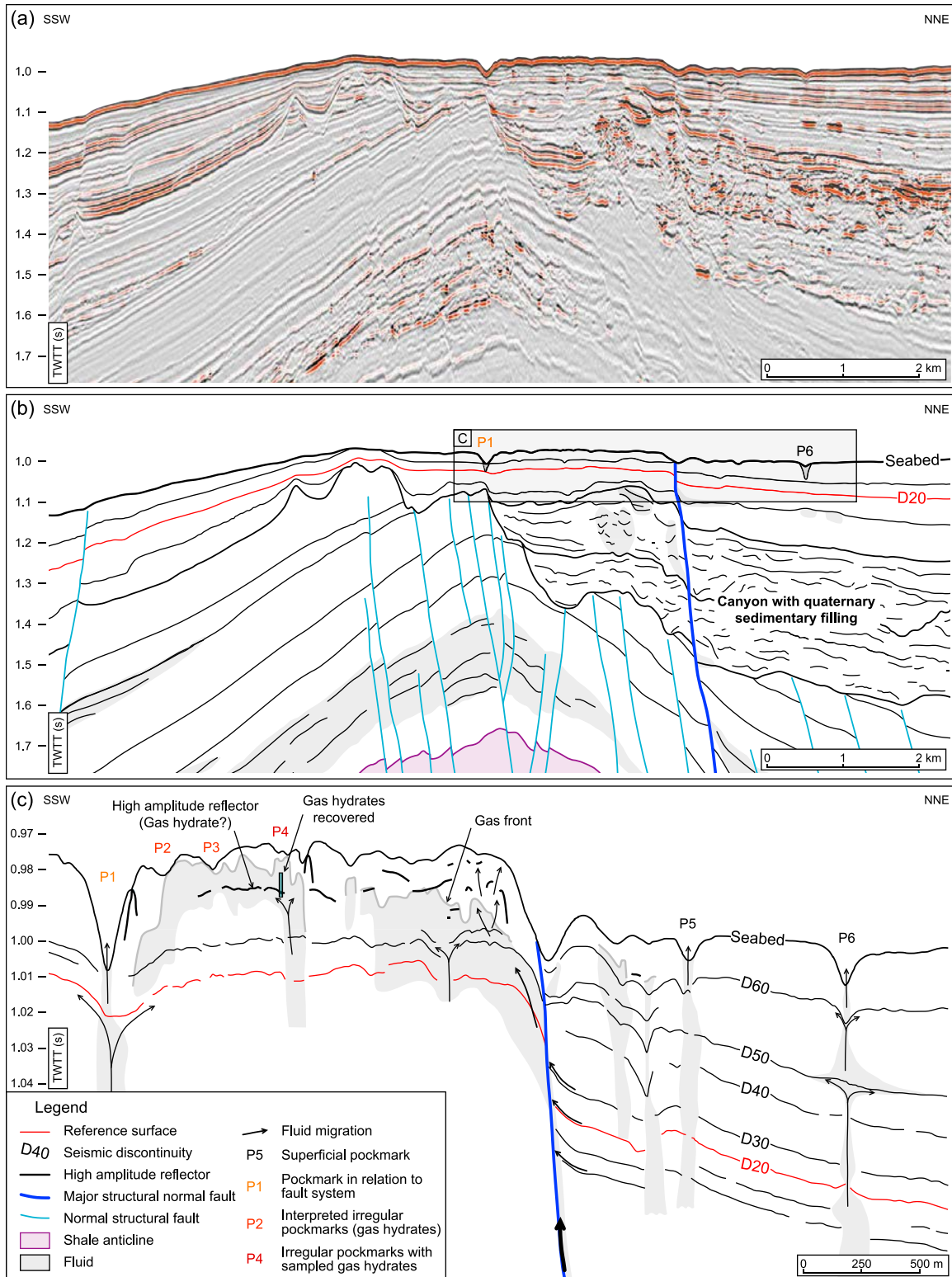
Figure 7. (a) Uninterpreted random line extract from 3-D high resolution (HR) seismic data showing the seismic morphology and stratigraphy under the irregular pockmarks area, the fluid reservoir, and fluid migration areas. (b) Seismic interpretation of the seismic line presented in 7a. (c) Interpretation of the seismic profile presented in Figure 3a. It is a seismic profile zoom of the upper part of the profile in Figure 7a (located by the dark rectangle in Figure 7b).
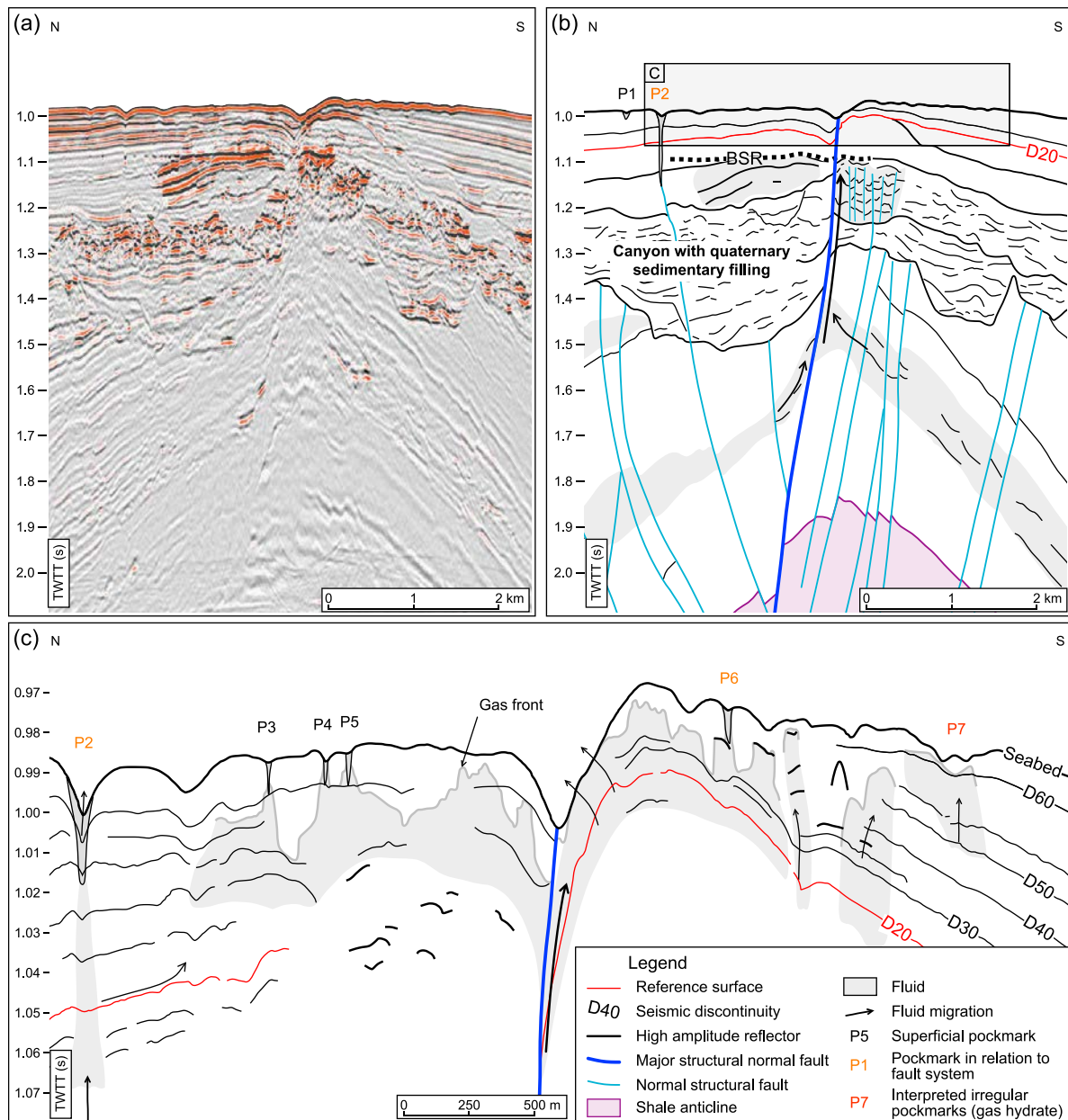
Figure 8. (a) Uninterpreted random line extract from 3-D HR seismic data showing the seismic morphology under the irregular pockmarks area, the fluid reservoir, and fluid migration areas. (b) Interpretation of the seismic line presented in 8a (BSR, bottom-simulating reflector). (c) Interpretation of the VHR seismic profile presented in Figure 3b. It is a seismic profile zoom of the upper part of the profile in Figure 8a (located by the dark rectangle in Figure 8b).

after 5 June 2008; then a sudden jump of 3 kPa is observed on 19 June, followed by a gradual increase until 5 July (except between 22 and 24 June, when a peak reaching a maximum of 13 kPa is observed). After 5 July 2008, the differential pore pressure decreases over 34 days, until 9 August 2010. At this date, a sudden increase in pore pressure is observed, followed by a diffusion-type decrease curve. It is important to mention the tidal cycles' effect on the differential pore pressure measured by PZS12/P5, which was amplified significantly after 19 June 2008. This is an indication of the increase of the compressibility of the pore fluid and, therefore, of the free gas content in the pore fluid

at the PZS12/P5 location after 19 June. Pore pressure fluctuations that are due to tidal activities can hypothetically be used to quantify the free gas content. However, gas exsolution and dissolution processes accompanying tidal activities depend strongly on the nature and the solubility of the gas [see, e.g., *Sobkowicz and Morgenstern*, 1984]. Because of the lack of such chemical data, these quantitative analyses about free gas content are not currently possible.

[21] Figure 10a presents, for PZS20, the initial impulsion and dissipation of the pore water pressure at the five sensor levels. Between 36 and 48 h were needed to reach the pore pressure equilibrium on all five sensors. For the upper four
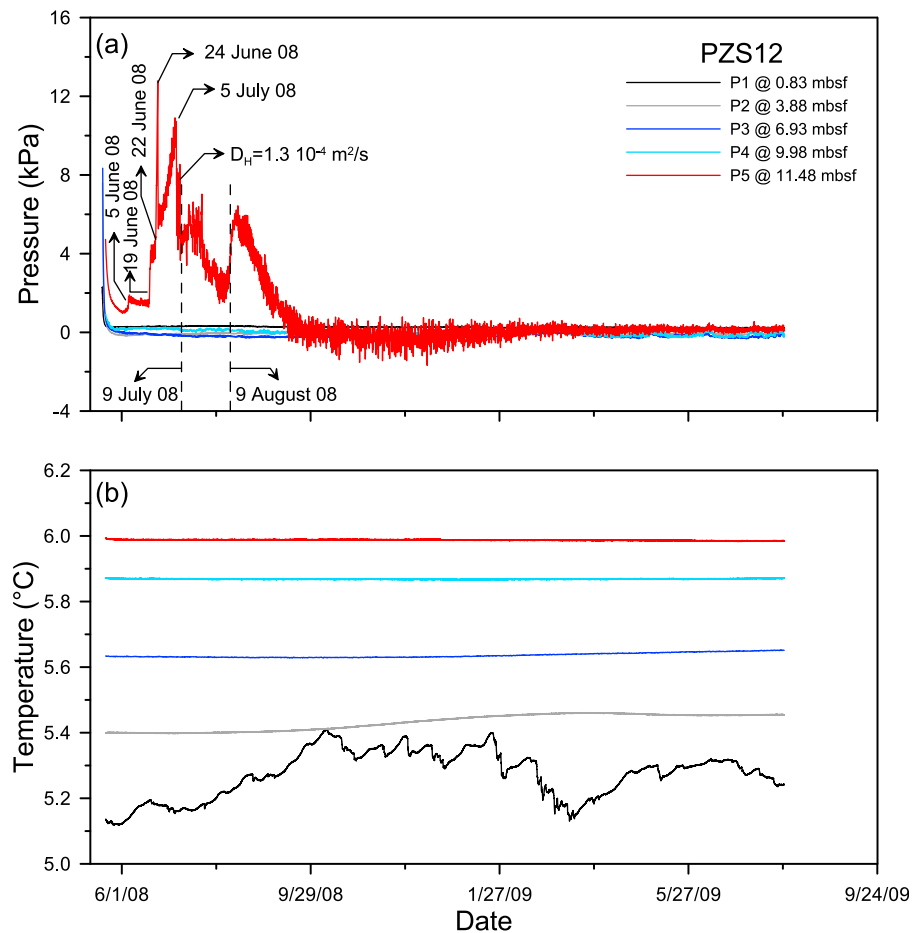
Figure 9. PZS12: (a) excess pore water pressure and (b) temperature versus time. For the upper four sensors (P1–P4), pore pressures remained almost constant until the end of the deployment. Pore pressure at P5 varies significantly with time (mainly after 5 June), indicating the highly dynamic character of the studied system.

sensors (P1–P4), pore pressures were almost constant until the end of recording (Figure 10a). For the fifth sensor of PZS20 (P5 at around 7.78 mbsf), the pore pressure drops slightly (by ~0.5 kPa below hydrostatic) on 9 July 2008. On 13 July 2008, a sudden drop is observed, by about 2 kPa. After this date, the pore pressure slightly varies (between 1 and 2 kPa below hydrostatic) until 9 August 2008, after which it recovers abruptly to hydrostatic pressure. The tidal activities effect on the differential pore pressure measured by PZS20/P5 was much more pronounced between 13 July and 9 August 2008, showing once again the increase of the compressibility of the pore fluid (and the increase of free gas content) during this transient period.

[22] The important pore pressure perturbations measured by PZS12 and PZS20 (Figures 9 and 10) at the base of the piezometer lances seem to diffuse very slowly vertically through the sedimentary column (see Appendix B). It is clear from the calculation presented in Appendix B that during the 1 year monitoring period, only a limited area surrounding the sensors P5 of PZS12 and PZS20 is affected by the pore pressure variations. Data from PZS12 and PZS20 confirm the influence of the fluid activities surrounding the major eastern fault. The main conduits of those fluid flows are the sandy-silty layers, as can be observed from Figure 5d for PZS12. Fluid circulations within the clayey sediments are only possible by hydrofracturing or by opening existing fractures as it was assumed from the reduced qt values on CPT12S06 location (Figure 6). Fluid flow seems to occur more laterally in the upper sedimentary layers (above PZS12/P5 and PZS20/P5) as the pore pressure accumulations were not accompanied by any temperature changes (Figure 9b).

4.2.4. Evidence From Microseismic Signatures

[23] The main objective of the OBS experiment was to establish a baseline of the microseismicity in the major eastern fault area of the study field. The experimental layout (Figure 1c) was chosen to ensure recording of microseismicity around the major eastern fault and with an instrument density sufficient to relocate the source position of events recorded eventually by four or more OBS. However, because of technical problems, the instruments stopped recording prematurely, and most instruments recorded only for 14 and 28 days after the deployment. During the recording period, the most significant microevents were detected on OBSs
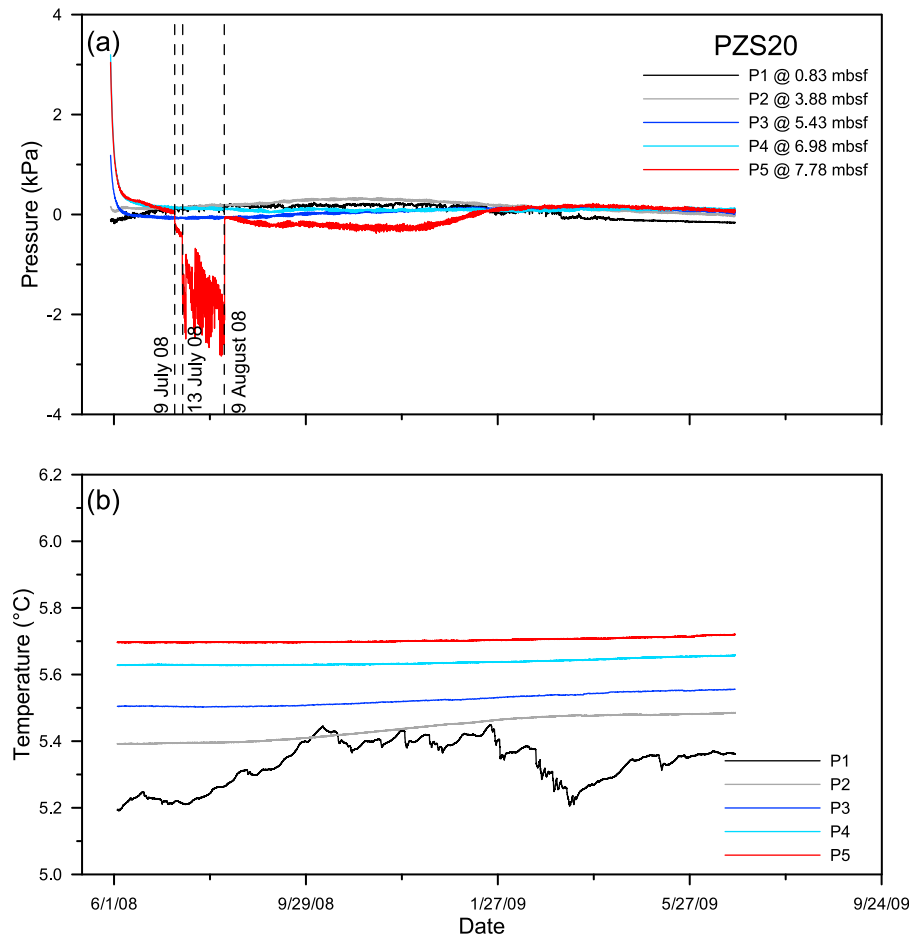
Figure 10. PZS20: (a) excess pore water pressure and (b) temperature versus time. For the upper four sensors (P1–P4), pore pressures were almost constant until the end of recording. For the fifth sensor (P5), the pore pressure varies with time (below hydrostatic) and mainly between 9 July and 9 August 2008.

04, 05, 07, and 08. OBS08 stopped recording on 11 June, while OBSs 05 and 04 stopped on 21 and 22 June, respectively. So, among these four instruments, OBS07 was the only one functioning after 22 June (OBS 07 did record until 15 August 2008).

[24] Although between 68 and 652 events were recorded by individual seismometers, no events were recorded by more than one instrument simultaneously, preventing the localization of microseismic events (Table E4). During the recording period, no earthquake (with arrivals recorded at different distant OBSs) was detected. Instead, the instruments recorded a great number of microevents having the following characteristics:

[25] 1. Microevents are frequent but not isolated; instead, they appear to occur as part of swarms, each swarm being made of a few tens of individual events.

[26] 2. There is no correlation between distant (1 km) OBSs.

[27] 3. The duration of each event is less than 300 to 400 ms, with frequencies ranging between 10 and 30 Hz; peak amplitudes are highly variable, between 0.5 and 20 μm/s. For comparison, in other deployments local earthquakes with moment magnitudes of 2 to 3 and distant by a few tens of

kilometers have been recorded on the OBSs with amplitudes of a few tens of micrometers per second.

[28] 4. The microevent signals are detected by all geophone components (x, y, z); only those microevents that have the largest amplitude are detected on the hydrophone.

[29] From the above, we conclude that the microevents recorded by the OBSs are not due to instrumental artifacts, nor are they related to biological (fish) activity. Instead, the results of a study conducted to identify similar signals from the Sea of Marmara ((J. B. Tary et al., personal communication, 2011) suggest the microevents are related to natural degassing processes from the seafloor or from the near subsurface.

5. Subsurface Thermal Regime

[30] The temperature measurements carried out at the PZS12 location show, for the shallowest sensor, relatively significant near-seafloor temperature changes (a maximum variation of 0.3°C at 0.83 mbsf) during the 1 year piezometer deployment (Figure 9b). The temperature changes measured at the four deeper sensors of PZS12 were less than 0.1°C (Figure 9b), rarely above the temperature sensor's resolution
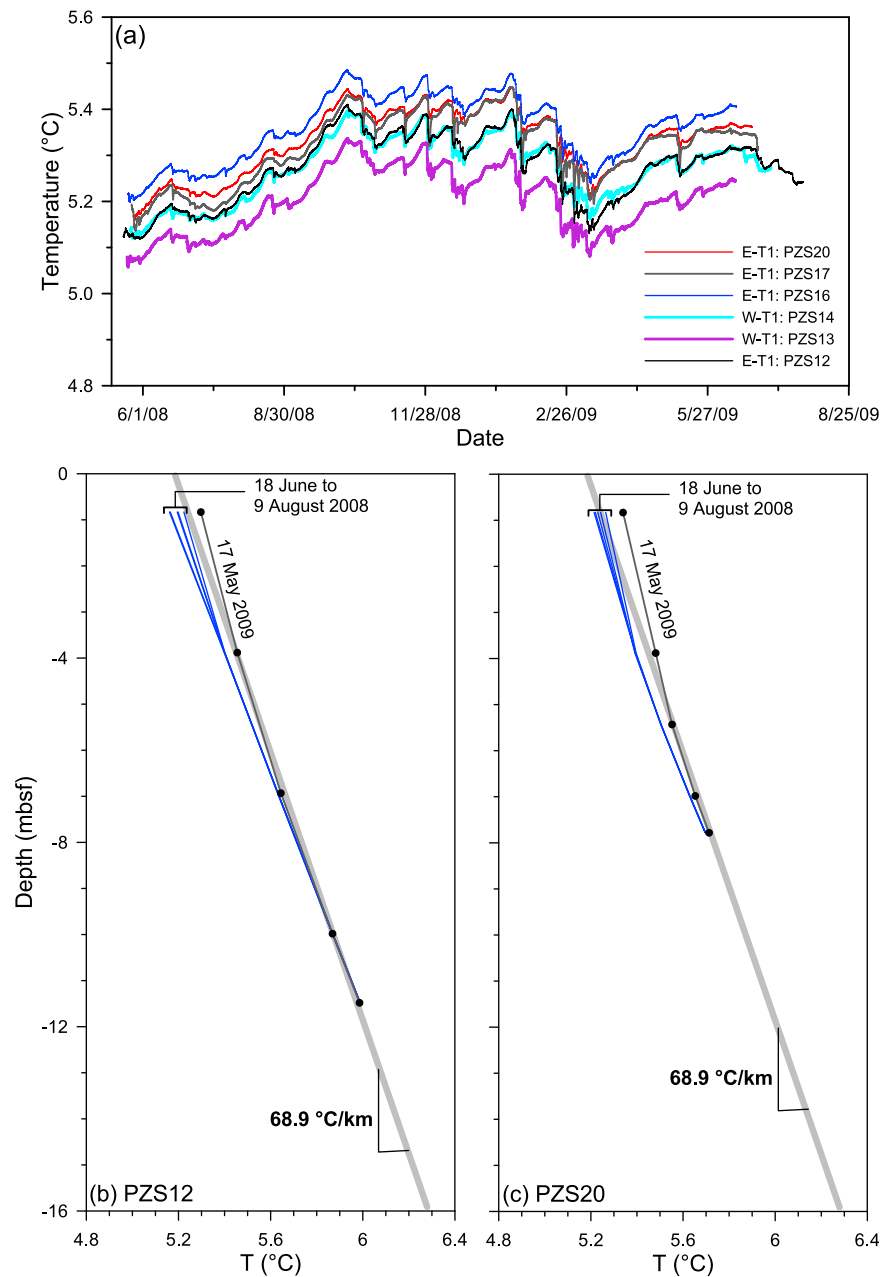
Figure 11. (a) Temperature histories (around 1 year) measured by the upper first sensor (between 0.83 and 0.92 mbsf) of six piezometers deployed surrounding the anticline. PZS13, PZS14, and PZS17 were deployed at water depths of 761, 753, and 736 m, respectively. PZS13 and PZS14 are positioned to the west of the anticline while the PZS17 is positioned to the east. Geothermal profiles recorded between 19 June 2008 and 17 May 2009 from (b) PZS12 and (c) PZS20. A supposed reference thermal gradient acquired at around 2.5 km to the northeast of PZS12 is also added to Figures 11b and 11c (light gray curve).

(0.05°C). The temperature measurements carried out at the PZS20 location indicate relatively significant seafloor temperature changes (a maximum variation of 0.3°C at 0.83 mbsf) (Figure 10b), again with far smaller changes at depth.

[31] Figure 11a shows the temperature evolution (around 1 year) measured by the upper first sensor (between 0.83 and 0.92 mbsf) of six piezometers deployed surrounding the anticline. The six piezometers were deployed at water depths between 736 and 761 m. PZS13 and PZS14 were positioned west of the anticline while PZS17 was positioned to the east.

Temperature fluctuations from the six piezometers presented in Figure 11a show similar seasonal variations with a similar range of variations during the 1 year monitoring. In addition, interseasonal fluctuations can be observed on the six piezometers' recordings. The temperature measured by the upper sensor of the six piezometers during the monitoring period is between 5.05°C and 5.5°C. The concordance between the temperature curves presented in Figure 11a shows that no large influence is exerted by a local process that could

perturb the seabed temperature field during the monitoring period.

[32] Figures 11b and 11c show geothermal profiles recorded by PZS12 and PZS20 between 19 June 2008 and 17 May 2009 compared with a supposed reference thermal gradient acquired at around 2.5 km to the northeast of PZS12. For the two piezometers, it can be concluded that the thermal transient regime is only linked to the seawater temperature changes without any input from an external mechanism that could perturb the geothermal profiles
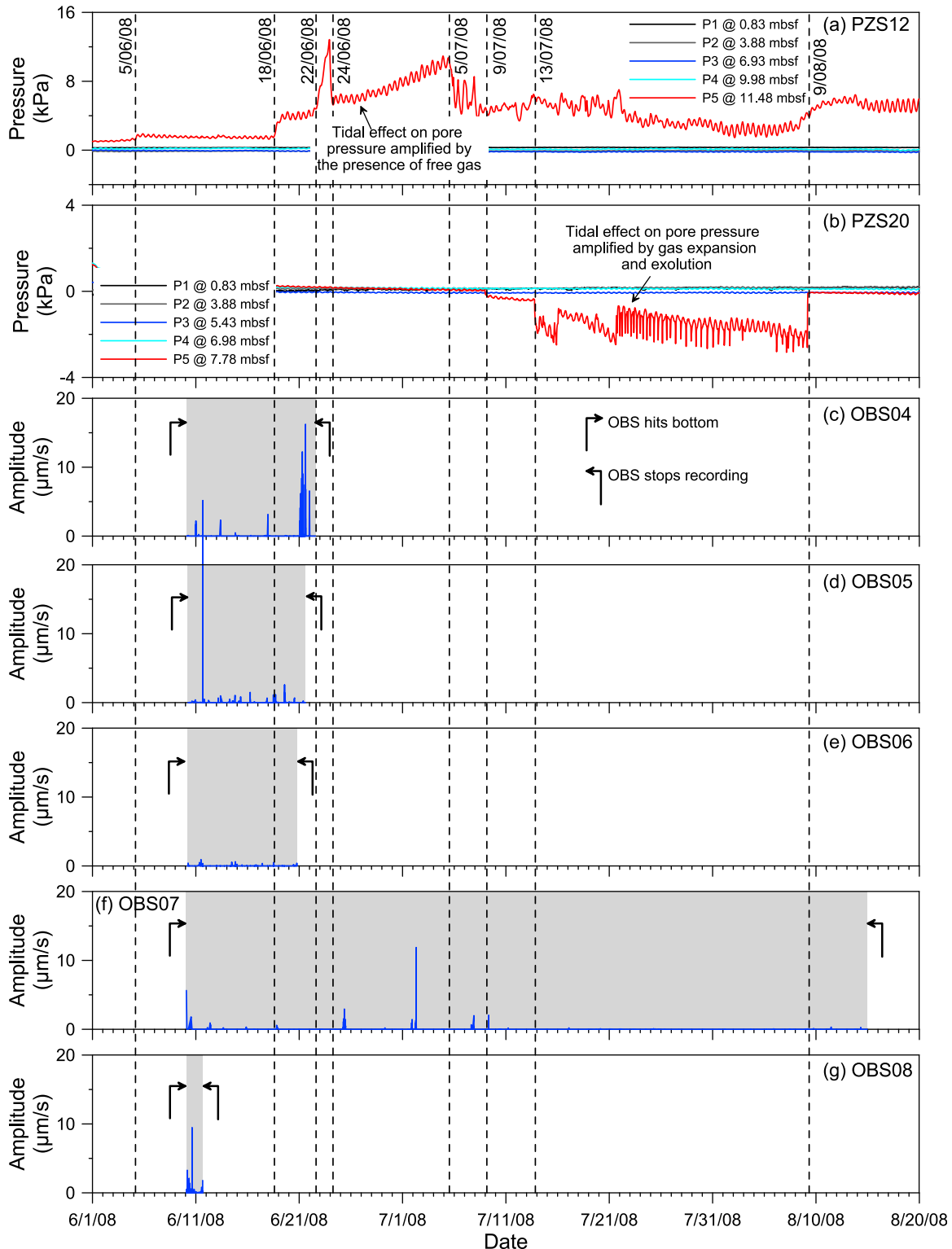

Figure 12

(Appendix A). Moreover, the pore pressure changes observed by PZS12 and PZS20 around 9 July 2008 did not produce any thermal perturbation.

6. Discussion: Faults, Microseismicity, Fluid Release, and Hydrate Distribution

[33] Figure 12 summarizes six measurements from PZS12, PZS20, OBS04, OBS05, OBS07, and OBS08. A small increase in differential pore pressure of 1 kPa is first recorded at PZS12 (sensor P5) on 5 June 2008. On 10 and 11 June, two small crises with microevents are detected on all four OBSs (Figures 12d–12g). Then, on 19 June, an abrupt increase in pore pressure is observed at PZS12 (sensor P5), followed by a regular, positive trend until 5 July (reaching 11 kPa). Superposed on this regular trend, a strong peak, reaching a maximum value of 13 kPa, occurs between 22 and 24 July, shortly after the most significant swarm in microevents detected by OBS4 between 21 and 22 June. After 5 July, the pore pressure decreases abruptly. On 9 August, a sudden increase in pore pressure is detected at PZS12, followed by a progressive recovery to hydrostatic (Figure 12a).

[34] The geometry of the sandy-silty layer below PZS12 pulls up to around 5 mbsf at the northern flank of the fault (Figure 8c) and can explain the sudden decrease of the pore pressure measured by PZS12/P5 on 24 June and 5 July 2008. Indeed, pore pressures of 13 kPa and 11 kPa correspond to around 82% and 70%, respectively, of the vertical effective stress at 5 mbsf (for a submerged mass density of 0.33 g/cm^3; see Figure A2). This high pore pressure is enough to create hydrofracturing or to open existing fractures in the overlying 5 m of clayey sediments (see Appendix D).

[35] In addition, hydrofracturing on the northern flank of the major eastern fault was already detected thanks to CPT12S06 (Figure 6). The hydraulic diffusivity D_H value was calculated from the dissipation curve, which took place after 5 July (see Figure 9). The hydraulic diffusivity D_H was found equal to 1.3×10^{-4} m^2/s for a drainage path of 5 m, corresponding to the depth of the sandy layer at the northern flank of the major eastern fault. This unusually high D_H value (4 orders of magnitude higher than the values presented in Appendix B) confirms that dissipation occurs through fractured sediments. On the other hand, the pore fluid accumulation that occurs on 9 August is followed by pore pressure dissipation with a hydraulic diffusivity comparable to the one presented in Appendix B. Indeed, the pressure of 6 kPa that had accumulated at the base of PZS12 by 9 August was not enough to open preexisting fractures, and the dissipation might have occurred with diffusion

through the clayey matrix. The presence of the free gas at PZS12/P5 position (after 19 June 2008) can be indirectly observed from the amplification of the tidal effect on pore pressure fluctuations and, therefore, on fluid compressibility and free gas content, as can be clearly seen from Figure 12a. On the basis of the PZS12 data, we propose that the migration of gas (in the sandy-silty layer that has been identified as a fluid conduit) results in the increase of pore pressure detected at 11.48 m below the seafloor at PZS12 after 5 June 2010. Gas accumulation in this layer near PZS12 site appears to be a nonsteady process with different phases: (1) continuous free gas flow and gas accumulation from 5 June to 5 July, with marked increases on 19 and 22 June, (2) hydrofracturing and/or open existing fractures and degassing phase starting on 5 July, (3) gas accumulation resuming abruptly on 9 August, eventually followed by a phase of fluid release with slow pressure recovery (diffusion) to hydrostatic.

[36] Pore pressure depression (pore pressure lower than the hydrostatic pressure) recorded at the PZS20 site (Figure 12b) occurs almost simultaneously with the decrease of the pore pressure measured at PZS12 location (5–9 July 2009). The end of the pore pressure depressions measured at the PZS20 site coincides with the second phase of pore pressure accumulation measured by PZS12 (9 August 2009). This pore pressure depression indicates that seawater penetrates into the bottom sediments at the level of PZS20. The origin of this depression could be a fast circulation of free gas in the sandy-silty layers. The expulsion of free gas generates two processes that may induce depressions in the surrounding medium: (1) a negative volume balance that is due to the fast gas bubble expulsion, and (2), depending on the gas velocities, a pressure depression can be created behind the gas bubbles. The decrease of the pore pressure recorded by PZS20/P5 is accompanied by gas exsolution and expansion, which increases the compressibility of the pore fluid and amplifies the pore pressure fluctuations under tidal cycles (Figure 12b).

[37] For the discussion hereafter, we recall our working hypothesis, in which the microevents measured by OBSs are related to degassing processes from the seafloor or from the near subsurface. The microevents recorded at one given OBS are not detected by the other OBSs, although they are located less than 750 m apart. This can be explained by assuming that the microevents are produced at very shallow depth (a few tens of meters) below the seafloor, in very attenuating sediments. This suggests that the nonseismic microevents originate in the immediate vicinity of the OBSs. The sources of the microevents recorded at the OBSs are too distant from PZS12 to be directly related to the degassing

Figure 12. Correspondence between piezometer records ((a) PZS12 (b) PS20) and OBS records ((c) OBS04, (d) OBS05, (e) OBS06, (f) OBS07, and (g) OBS08). The locations of the different instruments are indicated in Figure 1. This figure suggests that PZS12 records two-phase episodes: During phase 1, from 5 June to 5 July 2008, gas accumulation results in pore pressure increase; during phase 2, from July 2008 to February 2009, pore pressure slowly returns to equilibrium,. Note that (1) microevents occur as the OBSs hit bottom after deployment at sea; (2) microevents recorded at different OBSs are not correlated; (3) the most prominent swarm of microevents occurs near OBS04 on 21–22 June 2008, and our analysis suggests that this swarm likely results from the release of gas that accumulated in excess in the subsurface sandy-silty layers; (4) a peak in pore pressure occurred during phase 1 between 22 and 24 June, suggesting a sudden injection of gas by hydrofracturing and/or opening of existing fractures. The free gas circulation expansion and exsolution (after 19 June 2008 for PZS12/P5 and between 13 July and 9 August 2008 for PZS20/P5) are evidenced by the amplification of the tidal effect on the fluctuation of the differential pore pressure that is due to the increase of the pore fluid compressibility.
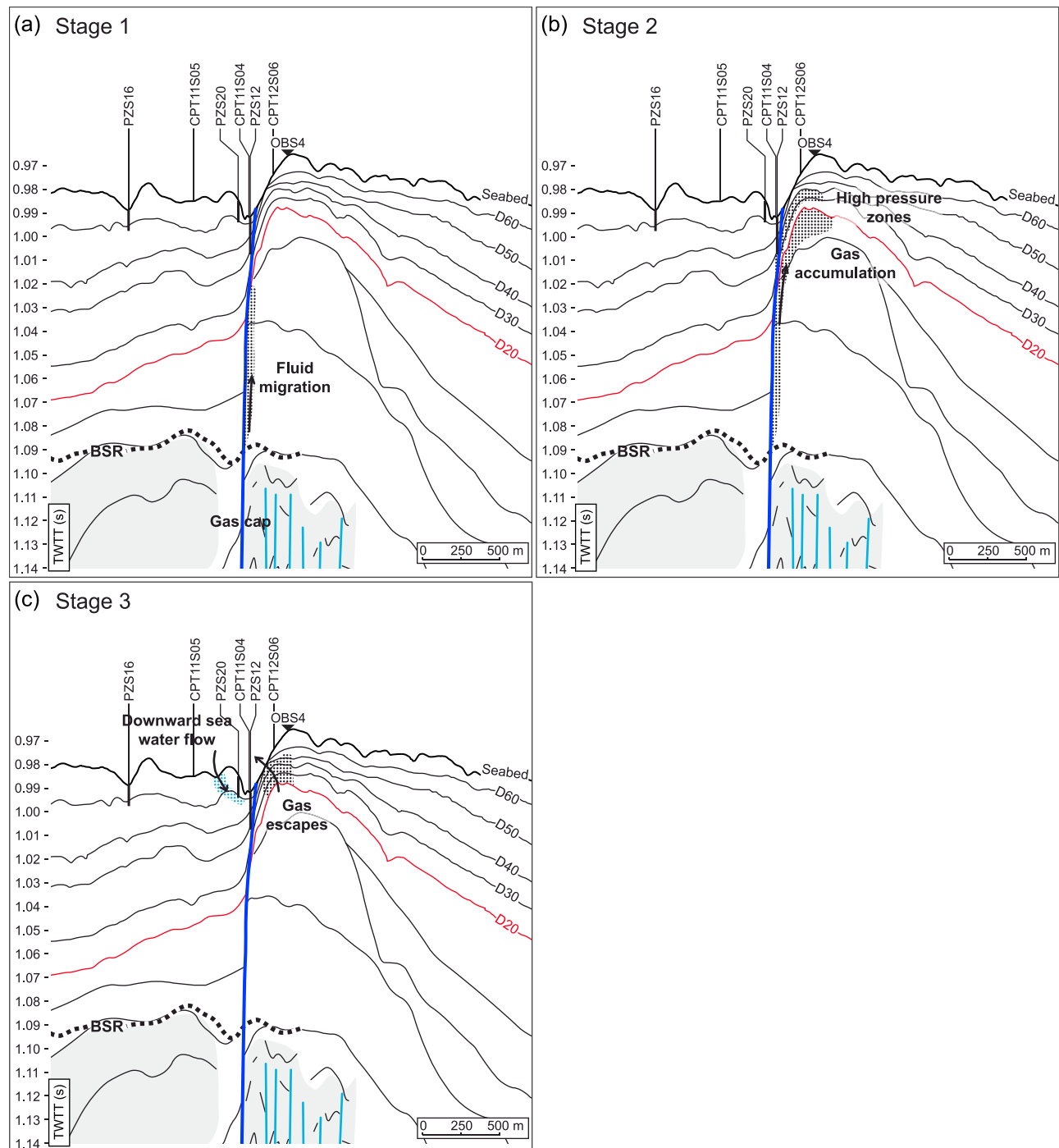
Figure 13. The studied hydrate-fault system operates according to the following three stages: (a) Stage 1: There is a slow upward pore fluid (mainly free gas) migration through existing conduits (mainly the major eastern fault) and free gas accumulation within several shallow sandy layers intersecting the major eastern fault. (b) Stage 2: Pore pressure increases within the sandy-silty layer, as evidenced by the data recorded at PZS12. (c) Stage 3: Hydrofracturing and fluid pressure dissipation occur through sporadic degassing events (with some of them being detected at the OBSs), eventually causing an interstitial water circulation through the shallow sandy layers and drawing overlying seawater into the sediment.

processes that could occur at the piezometer site, even though one can suspect that a causal, indirect relationship could exist between the microevents swarm detected on OBS04 between 21 and 22 June and the peak in pore pressure recorded at PZS12 on 23 and 24 June. To obtain the full picture of the relationships between the pore pressure and the microseismic events, the exact collocation of OBSs and piezometers is required.

[38] However, altogether the OBSs provide valuable information at the scale of the formation. The data indicate

that gas migration processes occur within the sandy-silty layer over a whole area centered on PZS12. These processes result in gas accumulation and increase in pore pressure at the PZS12 site, within the permeable sandy-silty layer, 11.48 m below the seafloor.

[39] The local process described in the present paper has some bearing on the dynamic systems presented by *Henry et al.* [1996] and *Tryon et al.* [1999] and is summarized in Figure 13 with the following three stages:

[40] 1. Slow upward pore fluid (mainly free gas) migration through existing conduits (mainly the major eastern fault) and free gas accumulation and circulation within several shallow sandy layers intersecting the major eastern fault.

[41] 2. Pore pressure increases within the sandy-silty layers as evidenced by the data recorded by PZS12. The free gas accumulation at these sandy layers was indirectly detected by the amplification of the effect of the tidal cycles on the recorded pore pressure fluctuations.

[42] 3. Hydrofracturing and/or opening existing fractures and fluid pressure dissipation through sporadic degassing events (with some of them being detected at the OBSs). This process can eventually cause interstitial water circulation through the shallow sandy layers and draw overlying seawater into the sediment (as was observed from PZS20/P5).

[43] Because of the geological complexity of the study area with the presence of several intermediate gas caps (Figure 7) and sandy-silty conduits, it is obvious that processes of free gas circulation, free gas accumulation, pore pressure increases, and degassing may occur simultaneously or separately at several locations surrounding the major eastern fault. This is supported by the several shallow chaotic facies that can be observed from the VHR seismic profiles presented in Figure 3 and the nonsynchronous microseismic events detected by the deployed OBSs (Figure 12). However, the good synchronization between the pore pressure dissipation at PZS12/P5 and the pore pressure decreases at PZS20/P5 raises the question about the important spatial extension and the time scale of such degassing phenomena and the potential link between gas hydrate distribution and fluid circulation processes. Indeed, gas hydrates were recovered by coring and indirectly detected by geophysical data and in situ geotechnical measurements to the south of the major eastern fault. Therefore, at a shallow depth below the seafloor, gas accumulation and fluid release seem to favor gas hydrate formation above sandy-silty conduits to the south of the fault, while the downward flow of seawater (seawater dilutes methane and avoids the formation of gas hydrates) prevents the accumulation of gas hydrates to the north of it. This observation can be drawn only for the upper explored sedimentary layers. The complexity of the piping system going from the main reservoir to intermediate gas caps through the major eastern fault and the sandy-silty conduits prevents any conclusion about the functioning of the deep system.

7. Conclusions

[44] In summary, seismic data, in situ geotechnical measurements, pore pressure, and temperature data presented here show that the studied fault-fluid-hydrate system is controlled by several transient regimes including pore fluid (mainly free gas) migration, free gas accumulation and pore pressure increases, degassing, and fluid pressure dissipation. This last phase can cause interstitial water circulation through the shallow sandy layers and draw overlying seawater into the sediment. The tidal activities' effect on the differential pore pressure that is directly linked to the increase of the compressibility of the pore fluid and the increase of free gas content have clearly demonstrated that migration and accumulation of free gases occur in silty sandy layers and hydrofractured clayey layers.

[45] At a shallow depth below the seafloor, gas accumulation and fluid release seem to favor gas hydrate formation above sandy-silty conduits to the south of the major eastern fault, while the downward flow of seawater prevents the accumulation of gas hydrates to the north of it. Although microseismologic data using OBSs allow the detection of individual degassing events, it is not clear whether pore pressure accumulations, hydrofracturing, and recorded microevents are directly linked. That is why further experiments with collocated OBSs and piezometers could provide important insight on the timing of natural degassing processes from the seafloor.

Appendix A: Coring Hydrates and Sandy-Silty Sediments

[46] A calypso core (CS16, 12.00 m long) was collected at the central part of the irregular morphology of the seafloor on the eastern anticline flank (location in Figure 1b). The CS16 core was recovered from above the horizontal reflector, indicated in Figure A1 as an indicator of the top of the GHOZ. From CS16, gas hydrates were recovered at different depths between 4 and 12 mbsf (Figure A2). Hydrates were distributed heterogeneously with depth. Gas hydrates recovered at 5 mbsf were less massive than those sampled between 10 mbsf and 11 mbsf. Figure A2a shows lithology and mass density versus depth curves measured using the MSCL logging device. This last curve shows the limit between water-saturated sediments and gas-hydrate-bearing sediments. Indeed, a large decrease of the mass density can be observed at this limit. This discontinuity in the density curve is due to the presence of gas hydrates and to the free gas exsolution occurring after core retrieval. Figure A2b presents photo images from two parts of the core showing the presence of massive gas hydrates in completely reworked sediment.

[47] A calypso core CS23 (23 m long) was collected during the ERIG3D cruise in an area far from the free gas perturbation areas, at the eastern periphery of the study site (location in Figure 1b). This reference core intersects the regional reflector D60 and shows that the high amplitude characterizing this reflector can be correlated to a silty layer between 16 to 17 mbsf (Figure A2c).

Appendix B: Hydraulic Regimes at Piezometer Locations

[48] Important pore pressure perturbations were measured by PZS12 and PZS20 at the base of the piezometer lances.
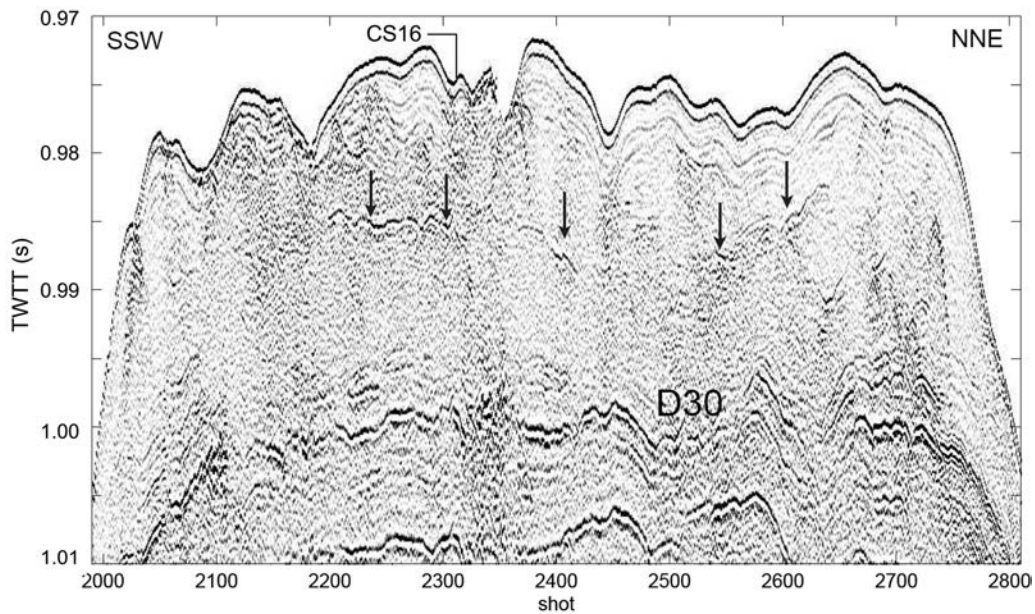
Figure A1. Zoom of seismic profile SY08THR-Pr05 showing a nonconsistent high-amplitude reflector that may correspond to the top of the gas hydrate occurrence zone (shown by arrows).

Durations of the pore pressure perturbation for PZS12 and PZS20 were, around 90 and 30 days, respectively. For the two piezometers, these pore pressure variations were localized at the level of the two lowest sensors, and none of the other eight sensors measured a significant pore pressure change during these perturbation periods. In order to check the validity of the pore pressure measurements and to evaluate theoretically the expected extension of these localized
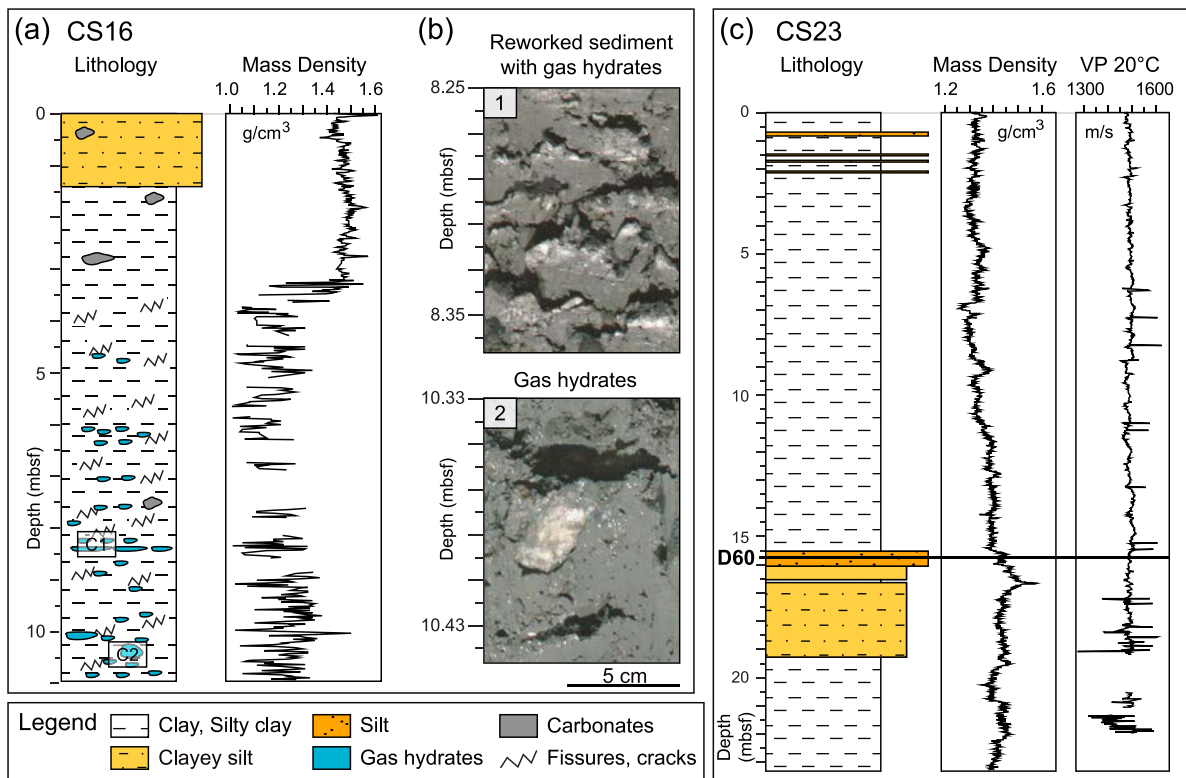

Figure A2. (a) Core CS16, log and mass density curve; (b) pictures of gas hydrates recovered from core CS16; (c) core log (CS23), density curve, and Vp laboratory-measured curve. The core description shows that reflector D60 corresponds to a silt layer.
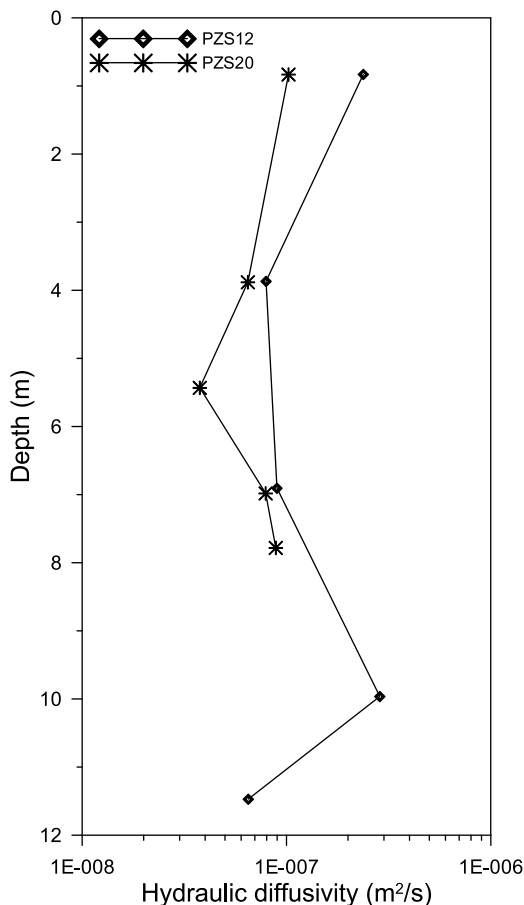
Figure B1. Hydraulic diffusivity values from PZS12 and PZS20 obtained from pore pressure dissipation curves.

pore pressure perturbations, a one-dimensional transient fluid flow is used:

$$\frac{\partial U(x,t)}{\partial t} = D_H \frac{\partial^2 U(x,t)}{\partial x^2} \qquad \text{(B1)}$$

where $U(x, t)$ is the pore pressure variable, D_H is the hydraulic diffusivity, t is the time ($t \geq 0$), and x ($0 \leq x \leq$ L) is the spatial variable. D_H values were derived from the pore pressure dissipation curves obtained after piezometer installation (Figure B1).

[49] The solution to equation (B1) requires specification of boundary conditions at $x = 0$ and $x = L$ and initial conditions at $t = 0$. For the case of the piezometer measurements, $U(L, t)$ was taken equal to the pressure measured at P5 and at the seafloor level, and $U(0, t)$ was taken equal to zero. Equation (B1) is numerically solved by approximating all the derivatives by finite differences and by using an explicit numerical method.

[50] Figure B2 shows the isocontours of the calculated pore pressure U at site PZS12 using the flow diffusion equation (equation (B1)) for a hydraulic diffusivity value of 5×10^{-8} m^2/s. At 11.48 mbsf, the imposed pore pressure U was taken from the P5 sensor of PZS12 (Figure 9a). The imposed pore pressure fluctuations diffuse very slowly through the sedimentary column for the considered D_H value. From Figure B2, it is clear that during the 1year period calculation, only an area of 1 m above sensor P5 is affected by the pore pressure variations. A similar calculation was carried out to simulate the extension of the pore pressure depression measured by PZS20 at P5. Again, the duration of the pore pressure perturbations measured at the base of PZS20 was not sufficiently important to diffuse and reach sensor P4.

Appendix C: Thermal Regimes at Piezometer Locations

[51] Temperature changes occurring in the upper sedimentary layers could be the result of the seafloor temperature fluctuations (diffusion) and/or water flow through highly permeable sediment (advection through faults and sandy layers). In order to identify the main thermal processes affecting the temperature field for the different studied sites, we consider as a working hypothesis that seafloor temperature changes are the main source of temperature fluctuations. In order to calculate the effect of these seafloor temperature
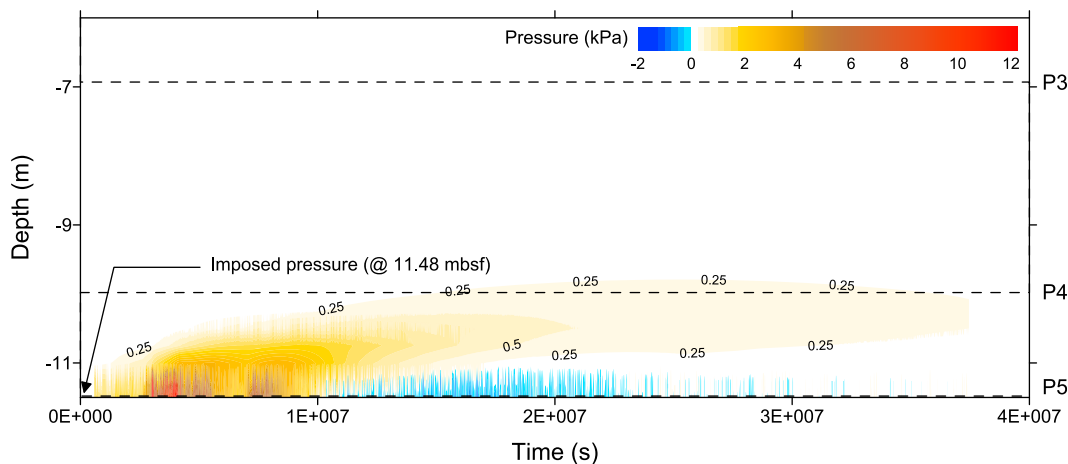

Figure B2. PZS12: Pressure perturbation imposed at the level of the last sensor (at 11.48 mbsf) and isocontours of calculated pore pressure using the diffusion equation for hydraulic diffusivity D_H equal to 5×10^{-8} m^2/s.

Figure C1. PZS12: Temperature changes imposed at the level of the first sensor (at 0.83 mbsf) and calculated temperature for the four other sensor levels and for three thermal diffusivity values. The calculated temperature changes are obtained by solving the heat equation in one dimension.
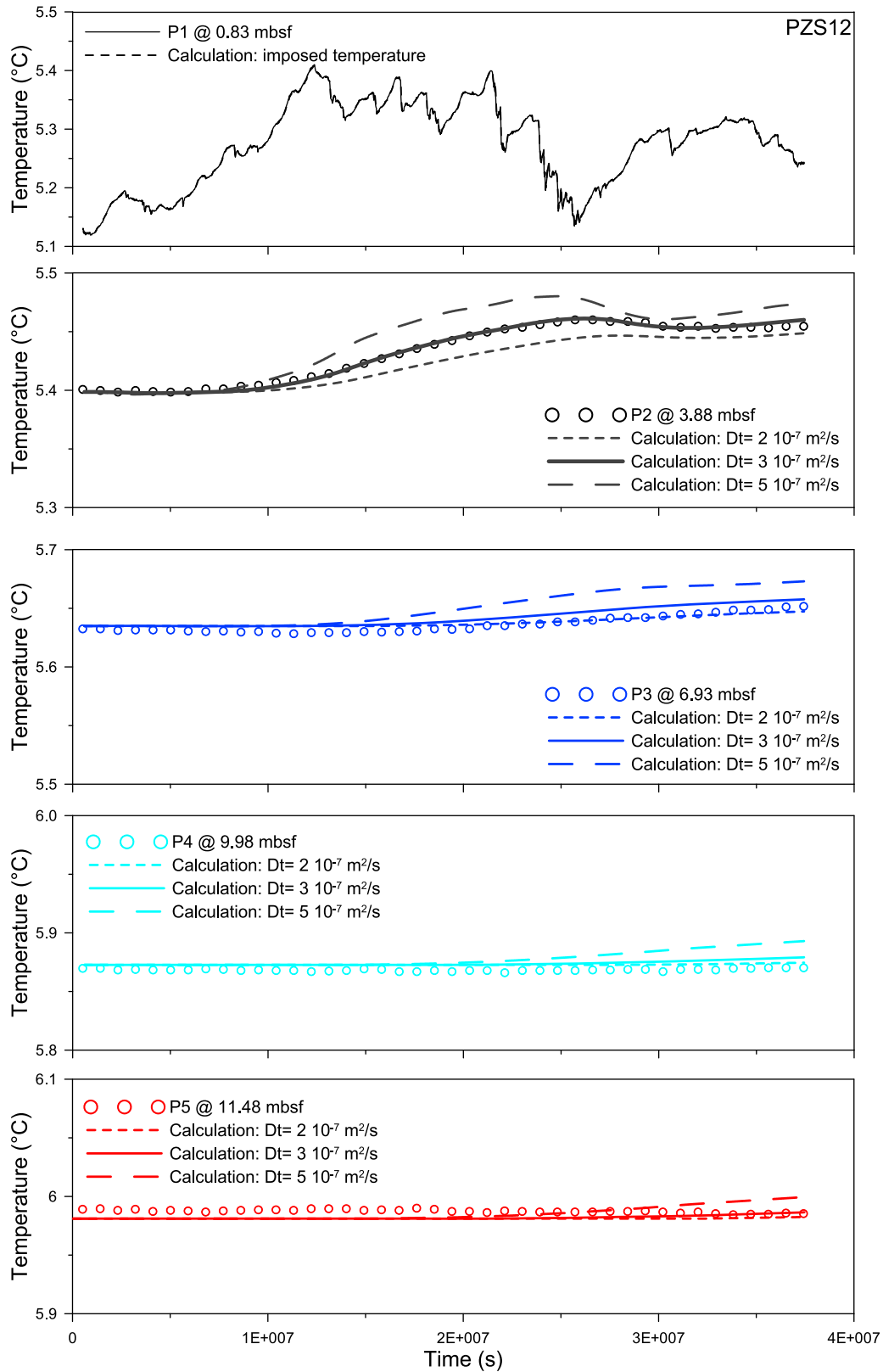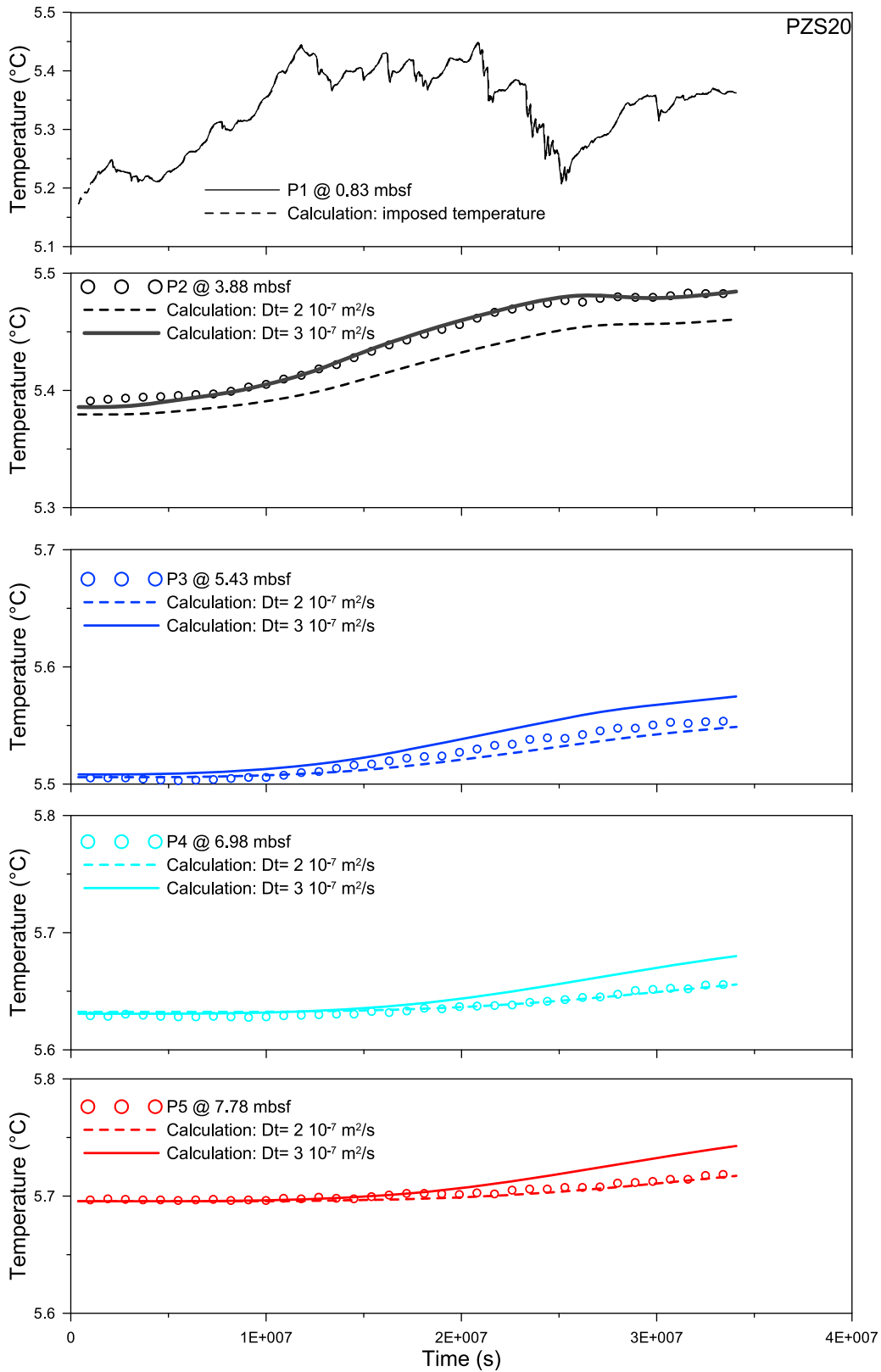
Figure C2. PZS20: Temperature changes imposed at the level of the first sensor (at 0.83 mbsf) and calculated temperature for the four other sensor levels and for two thermal diffusivity values. The calculated temperature changes are obtained by solving the heat equation in one dimension.

Table E1. Calypso Core Characteristics

	Tool	Core Length (m)	Bathy (m)	Deployed[a]	Observation
CS16	Calypso	14.00	731	16/05/08	Hydrates at the base
CS23	Calypso	23.28	786	27/05/08	Silty layer at around 16 m

[a]Read date as DD/MM/YY.

changes on the different deeper temperature sensors, we use the heat equation, which is given by

$$\frac{\partial T}{\partial t} = D_T \frac{\partial^2 T}{\partial x^2}, \tag{C1}$$

where $T = T(x, t)$ is the temperature variable, D_T is the thermal diffusivity, t is the time $(t \geq 0)$ and x $(0 \leq x \leq L)$ is the space variable.

[52] The solution to equation (C1) requires specification of boundary conditions at $x = 0$ and $x = L$ and initial conditions at $t = 0$. For the case of the piezometer measurements, $T(0, t)$ was taken equal to the temperature measured at P1 (upper first sensor) and $\frac{\partial T(L,t)}{\partial x}$ was taken equal to the mean temperature gradient measured in the area (Figure 11b). Equation (C1) is numerically solved by approximating all the derivatives by finite differences and by using an explicit numerical method.

[53] A comparison of the measured and calculated temperatures at the level of the four deepest sensors from PZS12 and PZS20 shows that for PZS12, the imposed temperature fluctuations diffuse very slowly through the sedimentary column for the three different D_T values (2×10^{-7} m^2/s, 3×10^{-7} m^2/s and 5×10^{-7} m^2/s) (Figure C1). These D_T values between 2×10^{-7} m^2/s and 5×10^{-7} m^2/s were derived from the temperature-time decay curves obtained after the PZS12 installation. A comparable D_T (equal to the thermal conductivity/heat capacity) value of 1.967×10^{-7} m^2/s was calculated from the mean porosity of the sediment (around 0.75; see Figure A2) and by considering a weighted harmonic mean sediment thermal conductivity (=0.741 W K^{-1}. m^{-1}) and an effective volumetric heat capacity (=3.767 $\times$ 10^6 J K^{-1} m^{-3}).

[54] From PZS12 (Figure C1) and PZS20 (Figure C2), it is clear that the temperature diffusion is the major process controlling the temperature in the upper sedimentary layers.

Table E2. Piezocone Characteristics

	Tool	Depth (mbsf)	Water Depth (m)	Deployed[a]	Observation
CPT11S01	CPTu	12.06	732	16/05/08	Early refusal
CPT11S02	CPTu	20.36	730	16/05/08	Early refusal
CPT11S03	CPTu	15.06	734	16/05/08	Early refusal
CPT11S04	CPTu	26.68	749	16/05/08	Early refusal
CPT11S05	CPTu	26.40	749	16/05/08	Early refusal
CPT11S06	CPTu	30.00	751	16/05/08	Ok – 30 m
CPT12S01	CPTu	9.74	731	18/05/08	Early refusal
CPT12S03	CPTu	19.90	733	18/05/08	Early refusal
CPT12S05	CPTu	30.00	736	18/05/08	Ok – 30 m
CPT12S06	CPTu	19.46	738	18/05/08	Early refusal
CPT15S02	CPTu	18.04	733	23/05/08	Early refusal

[a]Read date as DD/MM/YY.

Table E3. Piezometers Characteristics

	Duration	Water Depth (m)	Deployed[a]	Sensors at (mbsf)
PZS12	435 days	746	19/05/08	P1–0.83
				P2–3.88
				P3–6.93
				P4–9.98
				P5–11.48
PZS20	393 days	744	26/05/08	P1–0.83
				P2–3.88
				P3–5.43
				P4–6.98
				P5–7.78

[a]Read date as DD/MM/YY.

Indeed, for a thermal diffusivity of 3×10^{-7} m^2/s the discrepancies between measured and calculated temperatures are significantly lower than the accuracy of the temperature sensors (0.05°C).

Appendix D: Fracture Developments in Clayey Sediments

[55] Hydrofracturing is supposed to occur in sediment whenever the excess pore pressure exceeds the effective least principal stress plus the tensile strength of the medium [see, e.g., *Alfaro and Wong*, 2001]. In a purely lithostatic situation, in which sediment is subject to no forces except those of gravity, the greatest effective stress should be vertical (σ'_v) and the least effective stress should be horizontal (σ'_h) [*Sibson*, 2003]. Thus, σ'_h can be calculated from the lateral Earth pressure coefficient at rest Ko through the following equation:

$$\sigma'_h = Ko.\sigma'_v. \tag{D1}$$

From the in situ measured sleeve friction and using the relationship proposed by *Masood and Mitchell* [1993], Ko is calculated to be between 0.56 and 0.63. The indirect tensile strength of saturated sediment is usually estimated to be one-eight to one-twelfth of unconfined compressive strength [*Schroeder*, 1972]. Based on geotechnical properties acquired from the study area, the tensile strength was considered in this work as equal to 10% of the vertical effective stress. Therefore, hydraulic fracturing in saturated clay is considered to occur at 75% of the vertical effective stress.

Appendix E

[56] Calypso cores, piezocones, piezometers, and OBS characteristics are given in Tables E1, E2, E3, and E4, respectively.

Table E4. OBSs Characteristics and Recording Period[a]

	Water Depth (m)	Recording Period
OBS04	734	10/06/2008 02:00–22/06/2008 14:22
OBS05	739	10/06/2008 02:00–21/06/2008 16:31
OBS06	743	10/06/2008 02:00–20/06/2008 18:40
OBS07	748	10/06/2008 02:00–15/08/2008 01:58
OBS08	716	10/06/2008 02:00–11/06/2008 16:14

[a]Natural Frequency of Geophones: 4.5 Hz; Sampling Frequency: 250 Hz.

References

Alfaro, M. C., and R. C. K. Wong (2001), Laboratory studies on fracturing of low-permeability soils, *Can. Geotech. J.*, *38*, 303–315, doi:10.1139/t00-096.

Bayon, G., C. Pierre, J. Etoubleau, M. Voisset, E. Cauquil, T. Marsset, N. Sultan, E. Le Drezen, and Y. Fouquet (2007), Sr/Ca and Mg/Ca ratios in Niger Delta sediments: Implications for authigenic carbonate genesis in cold seep environments, *Mar. Geol.*, *241*, 93–109, doi:10.1016/j.margeo.2007.03.007.

Bilotti, F., and J. H. Shaw (2005), Deep-water Niger Delta fold and thrust belt modeled as a critical-taper wedge: The influence of elevated basal fluid pressure on structural styles, *AAPG Bull.*, *89*(11), 1475–1491, doi:10.1306/06130505002.

Bøe, R., L. Rise, and D. Ottesen (1998), Elongate depressions on the southern slope of the Norwegian trench (Skagerrak): Morphology and evolution, *Mar. Geol.*, *146*, 191–203, doi:10.1016/S0025-3227(97)00133-3.

Brooks, J. M., W. R. Bryant, B. B. Bernard, and N. R. Cameron (2000), The nature of gas hydrates on the Nigerian continental slope, in *Gas Hydrates: Challenges for the Future*, pp. 76–93, New York Acad. Sci., New York.

Cohen, H. A., and K. McClay (1996), Sedimentation and shale tectonics of the northwestern Niger Delta front, *Mar. Pet. Geol.*, *13*(3), 313–328, doi:10.1016/0264-8172(95)00067-4.

Corredor, F., J. H. Shaw, and F. Bilotti (2005), Structural styles in the deep-water fold and thrust belts of the Niger Delta, *AAPG Bull.*, *89*(6), 753–780, doi:10.1306/02170504074.

Damuth, J. E. (1994), Neogene gravity tectonics and depositional processes on the deep Niger Delta continental margins, *Mar. Pet. Geol.*, *11*(3), 320–346, doi:10.1016/0264-8172(94)90053-1.

Deptuck, M. E., G. S. Steffens, M. Barton, and C. Pirmez (2003), Architecture and evolution of upper fan channel-belts on the Niger Delta slope and in the Arabian Sea, *Mar. Pet. Geol.*, *20*(6–8), 649–676, doi:10.1016/j.marpetgeo.2003.01.004.

Doust, H., and E. Omatsola (1990), Niger Delta, in *Divergent/Passive Margin Basins*, edited by J. D. Edwards and P. A. Santogrossi, *AAPG Mem.*, *48*, 201–238.

Georges, R. A., and E. Cauquil (2007), AUV ultrahigh-resolution 3D seismic technique for detailed subsurface investigations, paper OTC18784, presented at the Offshore Technology Conference, Soc. of Pet. Eng., Houston, Tex.

Haskell, N., et al. (1999), *Delineation of geologic drilling hazards using 3-D seismic attributes*, *Leading Edge*, *18*, 373–382.

Henry, P., et al. (1996), Fluid flow in and around a mud volcano field seaward of the Barbados accretionary wedge: Results from Manon cruise, *J. Geophys. Res.*, *101*(B9), 20,297–20,323, doi:10.1029/96JB00953.

Hovland, M., J. W. Gallagher, M. B. Clennell, and K. Lekvam (1997), Gas hydrate and free gas volumes in marine sediments: Example from the Niger Delta front, *Mar. Pet. Geol.*, *14*(3), 245–255, doi:10.1016/S0264-8172(97)00012-3.

Ker, S., B. Marsset, S. Garziglia, Y. Le Gonidec, D. Gibert, M. Voisset, and J. Adamy (2010), High-resolution seismic imaging in deep sea from a joint deep-towed/OBH reflection experiment: Application to a mass transport complex offshore Nigeria, *Geophys. J. Int.*, *182*, 1524–1542, doi:10.1111/j.1365-246X.2010.04700.x.

Marsset, T., B. Marsset, S. Ker, Y. Thomas, and Y. Le Gall (2010), High and very high resolution deep-towed seismic system: Performance and examples from deep water geohazard studies, *Deep Sea Res., Part I*, *57*(4), 628–637, doi:10.1016/j.dsr.2010.01.001.

Masood, T., and J. K. Mitchell (1993), Estimation of in-situ lateral stresses in soils by cone-penetration test, *J. Geotech. Eng.*, *119*(10), 1624–1639, doi:10.1061/(ASCE)0733-9410(1993)119:10(1624).

Morley, C. K., and G. Guerin (1996), Comparison of gravity-driven deformation styles and behavior associated with mobile shales and salt, *Tectonics*, *15*(6), 1154–1170, doi:10.1029/96TC01416.

Papatheodorou, G., T. Hasiotis, and G. Ferentinos (1993), Gas-charged sediments in the Aegean and Ionian Seas, Greece, *Mar. Geol.*, *112*, 171–184, doi:10.1016/0025-3227(93)90167-T.

Riboulot, V., A. Cattaneo, V. Lanfumey, M. Voisset, and E. Cauquil (2011), Morphological signature of fluid flow seepage in the eastern Niger submarine deltas, paper OTC21744, presented at the Offshore Technology Conference, Soc. of Pet. Eng., Houston, Tex.

Schroeder, C. (1972), Influence of lithology on the mechanical behaviour of rocks in uniaxial compression and Brazilian tests, *Eng. Geol.*, *6*, 31–42, doi:10.1016/0013-7952(72)90023-3.

Sibson, R. H. (2003), Brittle-failure controls on maximum sustainable overpressure in different tectonic regimes, *AAPG Bull.*, *87*(6), 901–908, doi:10.1306/01290300181.

Sobkowicz, J. C., and N. R. Morgenstern (1984), The undrained behaviour of gassy sediments, *Can. Geotech. J.*, *21*, 439–448, doi:10.1139/t84-048.

Sultan, N., M. Voisset, T. Marsset, A. M. Vernant, E. Cauquil, J. L. Colliat, and V. Curinier (2007), Detection of free gas and gas hydrate based on 3D seismic data and cone penetration testing: An example from the Nigerian Continental Slope, *Mar. Geol.*, *240*, 235–255, doi:10.1016/j.margeo.2007.02.012.

Sultan, N., et al. (2010), Hydrate dissolution as a potential mechanism for pockmark formation in the Niger delta, *J. Geophys. Res.*, *115*, B08101, doi:10.1029/2010JB007453.

Tryon, M. D., K. M. Brown, M. E. Torres, A. M. Trehu, J. McManus, and R. W. Collier (1999), Measurements of transience and downward fluid flow near episodic methane gas vents, Hydrate Ridge, Cascadia, *Geology*, *27*(12), 1075–1078, doi:10.1130/0091-7613(1999)027<1075:MOTADF>2.3.CO;2.

Zhang, C., X. N. Xie, T. Jiang, and X. F. Liu (2006), Hydrocarbon migration and accumulation along a long-term growth fault: Example from the BZ25–1 oilfield of Bohai basin, eastern China, *J. Geochem. Explor.*, *89*(1–3), 460–464, doi:10.1016/j.gexplo.2005.11.032.

J. Adamy, Total, F-92078 Paris, La Défense CEDEX, France.

J. L. Colliat and S. Grimaud, Total, F-64018 Pau, CEDEX, France.

L. Géli, S. Ker, F. Klingelhoefer, V. Lanfumey, B. Marsset, V. Riboulot, N. Sultan, J. B. Tary, and M. Voisset, Département Géosciences Marines, Ifremer, BP 70, F-29280 Plouzané, France. (nabil.sultan@ifremer.fr)